ESA CONTRACT REPORT

Contract Report to the European Space Agency

Tech Note - Phase II - WP1100
SMOS Monitoring Report
Number 3: Dec 2011 - Dec 2012

Joaquín Muñoz Sabater,
Mohamed Dahoui,
Patricia de Rosnay,
Lars Isaksen

ESA/ESRIN Contract
4000101703/10/NL/FF/fk

European Centre for Medium-Range Weather Forecasts
Europäisches Zentrum für mittelfristige Wettervorhersage
Centre européen pour les prévisions météorologiques à moyen terme

ECMWF

Series: ECMWF ESA Project Report Series

A full list of ECMWF Publications can be found on our web site under:
http://www.ecmwf.int/publications/

Contact: library@ecmwf.int

European Centre for Medium Range Weather Forecasts
Shinfield Park, Reading, RG2 9AX, England

Contract Report to the European Space Agency

Tech Note - Phase II - WP1100
SMOS Monitoring Report
Number 3: Dec 2011 - Dec 2012

Authors: Joaquín Muñoz Sabater,
Mohamed Dahoui,
Patricia de Rosnay,
Lars Isaksen

Technical Note - Phase-II - WP1100
Monitoring Report Number 3: Dec 2011 - Dec 2012
ESA/ESRIN Contract 4000101703/10/NL/FF/fk

European Centre for Medium-Range Weather Forecasts
Shinfield Park, Reading, Berkshire, UK

April 2013

	Name	Company
First version prepared by (April 2013)	J. Muñoz Sabater	ECMWF
Quality Visa	E. Källén	ECMWF
Application Authorized by		ESA/ESTEC

Distribution list:

ESA/ESRIN
Luc Govaert
Susanne Mecklenburg
Steven Delwart
ESA ESRIN Documentation Desk

SERCO
Raffaele Crapolicchio

ESA/ESTEC
Tania Casal
Matthias Drusch
Klaus Scipal

ECMWF
HR
Division & Section Heads

Contents

Abstract

Contracted by the European Space Agency (ESA), the European Centre for Medium-Range Weather Forecasts (ECMWF) is involved in global monitoring and data assimilation of the Soil Moisture and Ocean Salinity (SMOS) mission data. For the first time, a new innovative remote sensing technique based on radiometric aperture synthesis is used in SMOS to observe soil moisture over continental surfaces and ocean salinity over oceans. Monitoring SMOS data (i.e. the comparison between the observed value and the model equivalent of that observation) is therefore of special interest and a requirement prior to assimilation experiments. This report is the third Monitoring Report delivered to ESA. The objective is to report on the monitoring activities of SMOS data over land and sea on a long term basis, investigating also the multi-angular and multi-polarised aspect of the SMOS observations. This report presents results for thirteen months (December 2011- December 2012) of SMOS data monitoring in Near Real Time obtained through the SMOS monitoring suite of ECMWF.

1 Introduction

ECMWF has developed an operational chain which monitors SMOS data in Near Real Time (NRT) at global scale, as explained in (12). Monitoring is carried out routinely for each new type of satellite data brought into the operational Integrated Forecasting System (IFS) at ECMWF. In Numerical Weather Prediction systems monitoring is mainly focused on the comparison between the observed variable and the model equivalent simulating that observation, because this is the quantity used in the analysis.
For SMOS, monitoring is produced separately for land and oceans. The reason is the strong contrast between the dielectric constant of water bodies and land surfaces, which in turn produces very different emissivities and observed brightness temperatures at the top of the atmosphere. Thus, monitoring SMOS data separately over land and oceans increases the sensitivity to the statistical variables. Moreover, the multi-angular and multi-polarised aspect of the observations is also accounted for in the monitoring chain by monitoring the data independently for several incidence angles of the observations and for two polarisation states at the antenna reference frame.
The developed framework makes it possible to obtain daily statistics of the observations, the model equivalent of the observations computed by the Community Microwave Emission Model (CMEM) (5; 3), and the difference between the two quantities, the so called first-guess departures. The statistics are computed over several weeks of data. This is a very robust way to identify systematic differences between modelled values and observations. Furthermore it also set the basis to investigate and understand the new observations before they become active in the ECMWF land assimilation scheme.

This Monitoring Report (MR3) on SMOS data is the third monitoring report delivered to ESA. In the first one (11) the monitoring website and statistical products were described. The second one (10) showed results obtained in NRT for the period November 2010- November 2011. This document monitors the period December 2011-December 2012. It follows the same strucuture than the previous report, allowing a better comparison with the statistics obtained in 2011.

2 SMOS observations at ECMWF

SMOS NRT products are processed at the European Space Astronomy Centre (ESAC) in Madrid (Spain) and sent to ECMWF via the SMOS Data Processing Ground Segment (DPGS) interface. The product used at ECMWF is the NRT product which are geographically sorted swath-based maps of brightness temperatures. The geolocated product received at ECMWF is arranged in an equal area grid system called ISEA 4H9 (Icosahedron Snyder Equal Area grid with Aperture 4 at resolution 9) [see (9)]. For this grid, the centre of the cell grids are at equal distance of 15 km over land, with a standard deviation of 0.9 km. For the NRT product, the resolution is coarser over oceans as they present lower heterogeneities that continental surfaces. The format of the NRT product is the Binary Universal Form for the Representation of meteorological data (BUFR). Each message in BUFR format corresponds to a snapshot where the integration time is 1.2 seconds. In average, each snapshot contains around 4800 subsets over land.

3 Monitoring over land

In this section some of the more relevant results obtained with the monitoring suite [see a description in part III of (12) and (11)] over land surfaces are shown.

3.1 Simulations of brightness temperatures

In order to simulate brightness temperatures at L-band and compare them to the SMOS observations, ECMWF has developed the Community Microwave Emission Model (CMEM) (4). It constitutes the forward model operator for low frequency passive microwave brightness temperatures of the surface. Although for SMOS purposes it is used at 1.4 GHz, potentially it can be used up to 20 GHz. This software package is fully coded in Fortran-90 language. It has been designed to be highly modular providing a good range of I/O interfaces for the Numerical Weather Prediction Community. CMEM surface forcing comes from the integration of the operational H-TESSEL (Hydrology Tiled ECMWF Scheme for Surface Exchanges over Land) land surface scheme [(1)]. H-TESSEL is forced with meteorological fields of surface pressure, specific humidity, air temperature and wind speed at the lowest atmospheric level. The surface radiation and precipitation flux represent 3 hourly averages, and they are kept constant over a 3 hour period. The integration of HTESSEL provides the soil moisture and soil temperature fields, as well as snow depth and snow density fields, which are then coupled with CMEM to simulate ECMWF first-guess L-band brightness temperatures. Additional land surface information needed is soil texture data obtained from the Food and Agriculture Organization (FAO) data set, whereas sand and clay fractions have been computed from a lookup table according to (15). The soil roughness standard deviation of height (σ) parameter in CMEM is set to 2.2 cm as in (7). Vegetation type is derived from the H-TESSEL classification, whereas a MODIS climatology is used to derive leaf area index (LAI).
CMEM's physics is based on the parameterisations used in the L-Band Microwave Emission of the Biosphere [LMEB, (17)] and Land Surface Microwave Emission Model [LSMEM, (6)]. The modular architecture of CMEM makes it possible to consider different parameterisations of the soil dielectric constant, the effective temperature, the roughness effect of the soil and the vegetation and atmospheric contribution opacity models. In the current configuration of CMEM, the vegetation opacity model of (8) is used, in combination with the (16) dielectric model, the (18) effective temperature model and the simple soil roughness model of (2). The atmospheric contribution is accounted for as in (14). This combination of parameterisations were shown to be well suited for brightness temperature modelling (5; 3; 13). However these results are based on local and regional scale experiments. A global sensitivity study with SMOS data has recently been conducted for assimilation purposes. The best CMEM configuration, in terms of best correlation with SMOS observed brightness temperatures for the year 2010, will be used from the coming ECMWF cycle 38R2, expected to be operational 25 June 2013. Therefore, it is expected an impact in the statistics.
Note also that CMEM is a SMOS Validation and Retrieval Teams (SVRT) tool freely available at *http://www.ecmwf.int/research/ESA_projects/SMOS/cmem/cmem_index.html*. More information about CMEM can be found in (4).

3.2 Time-averaged geographical mean fields.

Fig. 1 and Fig. 2 show the brightness temperatures as a function of the incidence angle for July 2012 and for six incidence angles multiples of 10, averaged in boxes of 0.25 degrees. Fig. 1 is for XX polarisation whereas Fig. 2 is for YY polarisation. These figures show very similar averaged values of brightness temperatures as those shown in the same figure of (10). Both polarisations behave as theoretically expected, i.e., brightness temperatures decreasing with the incidence angle for XX polarisation (from the averaged 240.1 K at 10 degrees to 219.7 K at 60 degrees) and increasing for YY polarisation (from the averaged 241.7 K at 10 degrees to 259.5 at 60 degrees). The same Hard Radio Frequency Interference (RFI) filter as in (11) was applied to the observed brightness temperatures, i.e., rejecting observations out of the [50,350] K interval. However, RFI is still present in some parts of Europe, and especially in Asia, and it contaminates the signal in other areas, thus obtaining many observations close to 350 K.
Fig. 3 shows the evolution of the SMOS observed brightness temperatures standard deviation at global scale, from January to October 2012 (one averaged value per month), at 40 degrees incidence angle and for XX polarisation. Fig. 4 is the equivalent figure for YY polarisation. These statistics are also computed in spatial boxes of 0.25 degrees. As explained in (10), most of the red colour observed in Europe and Asia is due to areas affected by RFI. Many of these sources of RFI are intermittent and they can contaminate large areas around the source. These plots still show strong sources in China and North of India, but also significant contamination in the Middle East and East of Europe. As it happened in 2011, the YY polarisation is in general more affected by RFI in regards to the extension of the affected area, mainly the North of China, however India is less affected in YY polarisation. In general, the situation in Western Europe is quite clean, as was reported too during 2011 (in 2010 Western Europe was one of the most affected areas by RFI). However, during summer 2012 the apparition of new very strong sources of RFI in Poland was reported (see more details in `https://earth.esa.int/c/document_library/get_file?folderId=234899\&name\discretionary{-}{}{}=DLFE-3603.pdf`). This can be clearly seen in the September and October 2012 plots of Fig. 3 and Fig. 4. For these months, the global mean standard deviation of the observations is increased, and likely explained by this extra sources of RFI. Also additional sources seem to affect strongly Europe in February 2011. America, Africa and Australia are little affected by RFI. These areas show good sensitivity to soil moisture variations and are important for assimilation experiments as they carry valuable information about soil moisture.

Figs. 5 and 6 show the evolution of the first-guess departures (observed brightness temperatures minus the CMEM model equivalents) at the antenna reference frame from January to October 2012 (one averaged value per month), at 40 degrees incidence angle and for XX and YY polarisations, respectively. The model clearly underestimates the observations in areas covered by snow and ice, especially for XX polarisation, which is a consequence of the not yet accurate representation of the model emissivity over these areas. The line of snow can be clearly followed in XX polarisation, as well as regions with strong orography (see for example the Himalayas chain in Fig. 5). The sensitivity to snow and ice in the YY polarisation is much weaker. In this case, a systematic negative bias is present as it happened in 2011, which partially is linked to the lack of variability of the roughness parameterisation used in CMEM for these plots. The bias observed in these figures are only for 40 degrees incidence angle, but they are different depending on the angle. This is discussed in section 3.4. The extraordinary underestimation of the observations in September and October 2012 of Figs. 5 and 6 is not due to natural causes, but this is a consequence of the new sources of RFI which showed up in summer 2012 in Poland.

The particular situation of RFI in Europe and the new RFI sources of Poland in summer 2012 are shown in Fig. 7. The punctual red dots observed in these plots, show large disagreement between the observations and the model, and are linked to fixed sources of RFI. The number of these dots are much reduced compared to the same figure of 2011 in (10). The efforts of the teams working on switching off sources of RFI in Europe can be appreciated in these plots. However, there are still remaining fixed sources, as for instance around London

in UK. Their intensity is limited and the contaminated area seems to be mainly constrained to the location of the source. The problems appeared in Poland in summer 2011 are clearly observed from August, but especially intense in September and October 2012, which contaminate most of Europe.

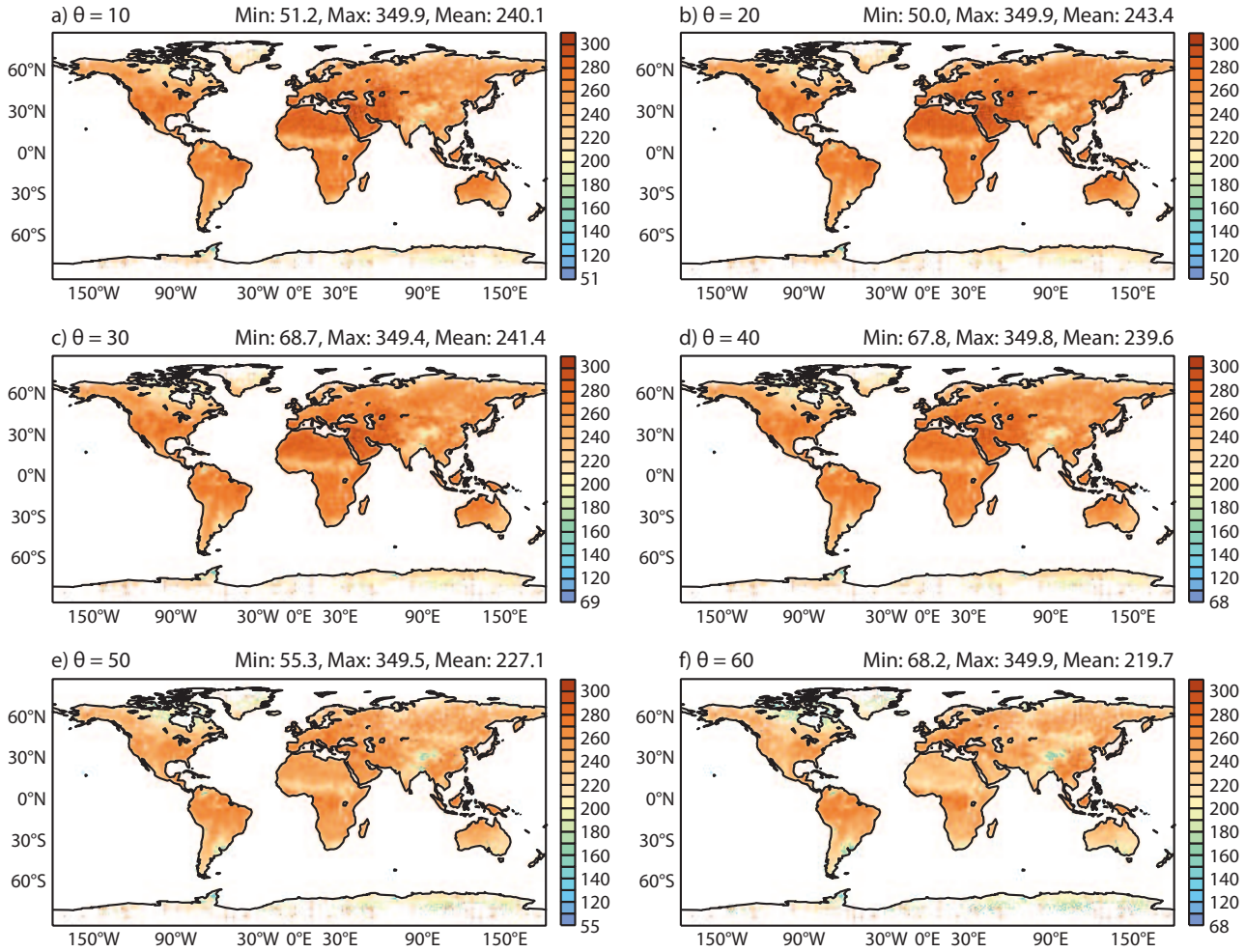

Figure 1: July 2012, geographical mean of the SMOS observed brightness temperatures as a function of the incidence angle, for XX polarisation. Each value represents a mean value of all the data inside a box of 0.25 degrees.

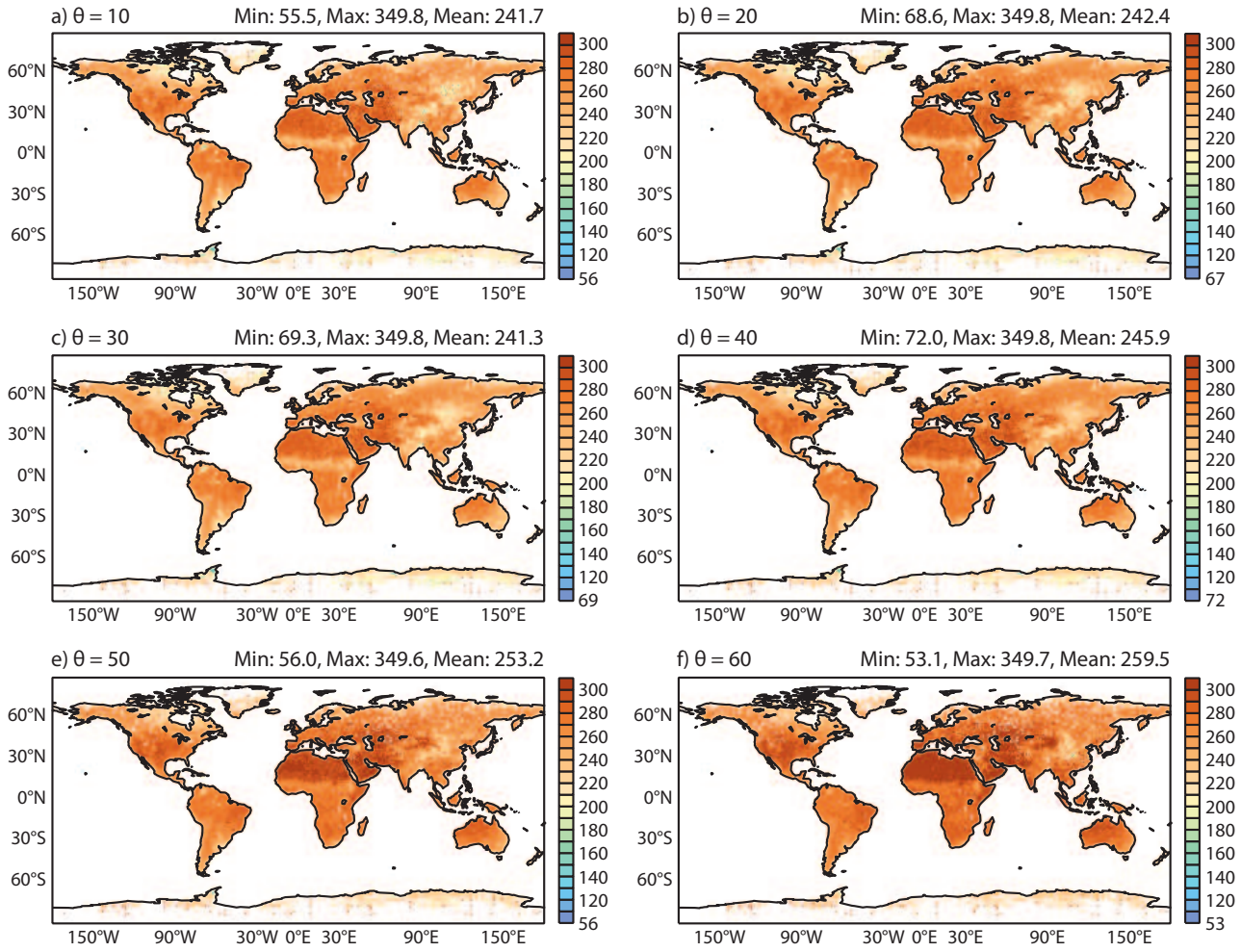

Figure 2: As in Fig. 1 but for YY polarisation.

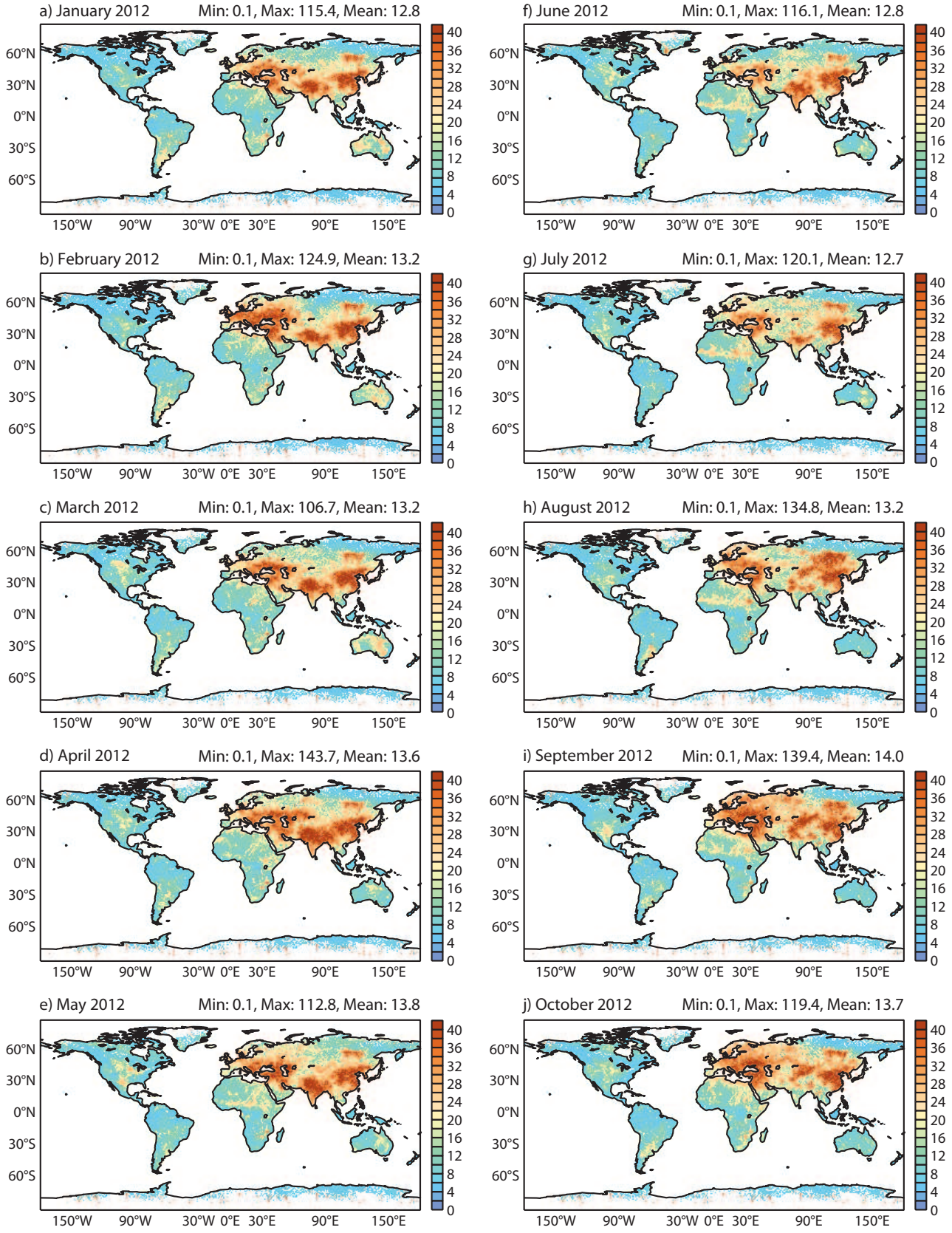

Figure 3: Monthly global mean of the SMOS observed brightness temperatures standard deviation, for XX polarisation, from January 2012 to Octobre 2012. Each value represents a mean value of all the data inside a box of 0.25 degrees. The incidence angle is 40 degrees.

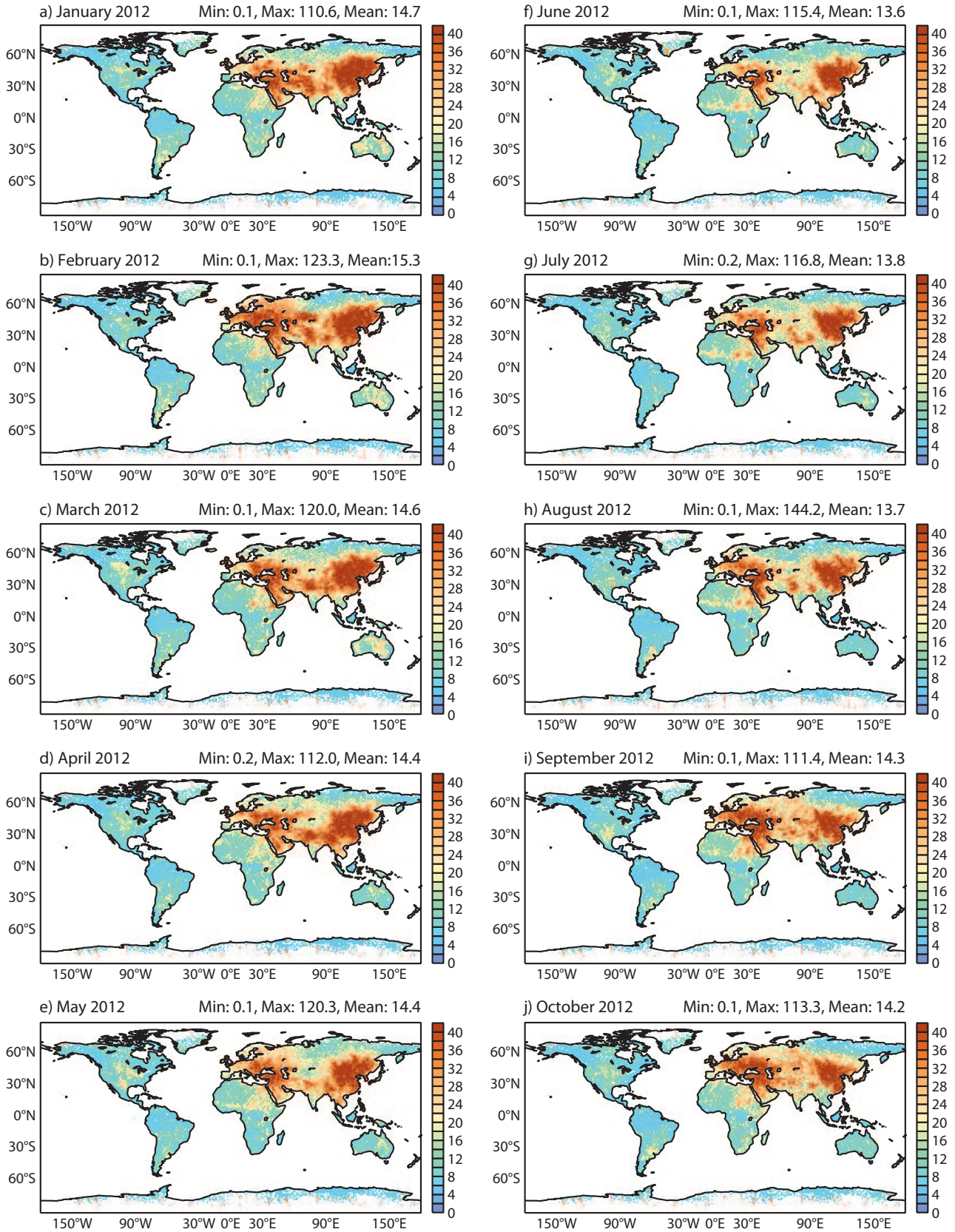

Figure 4: As Fig. 3, but for YY polarisation.

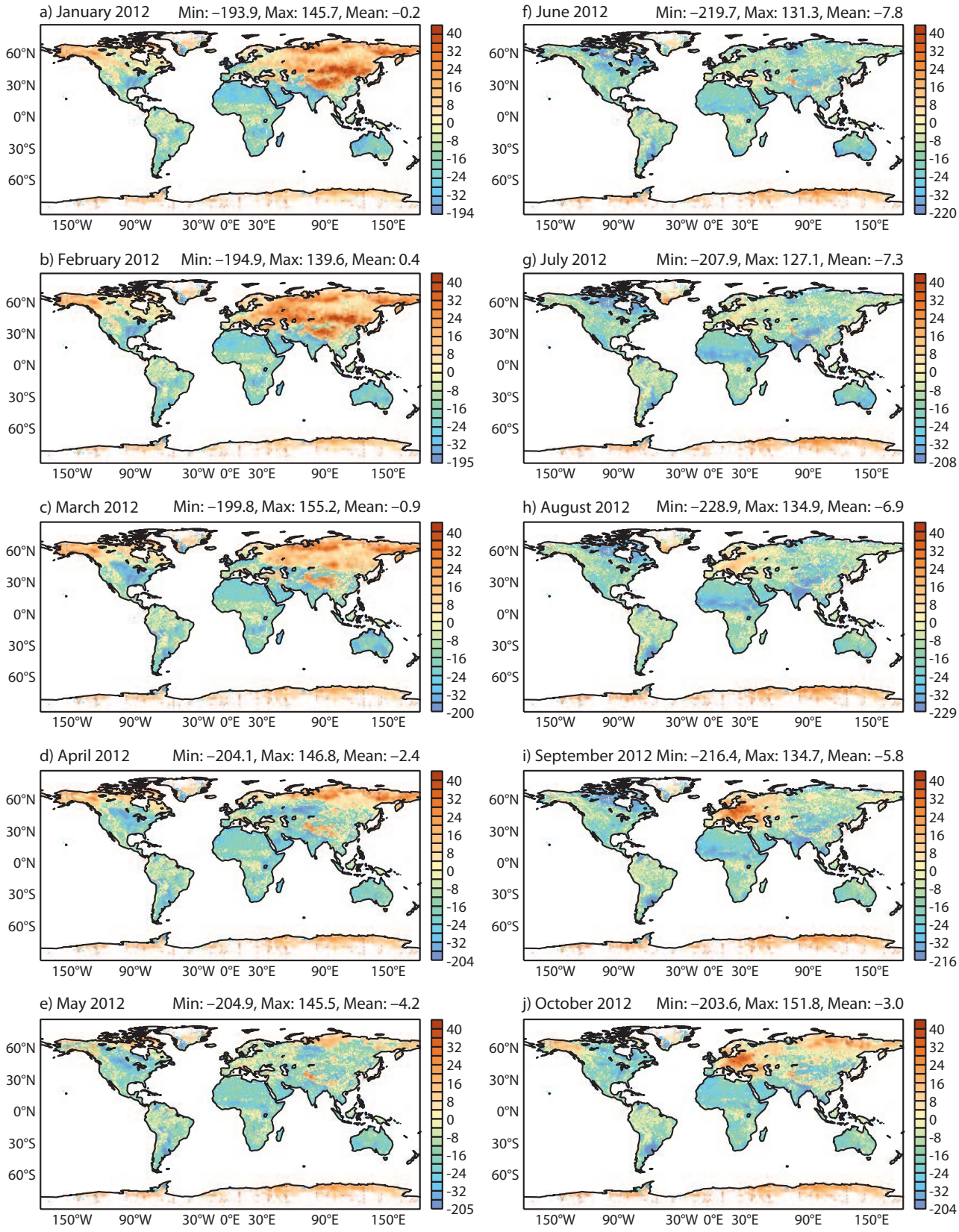

Figure 5: Monthly global mean of the first-guess departures between SMOS observed brightness temperatures and the CMEM model equivalents, for XX polarisation at 40 degrees incidence angle.

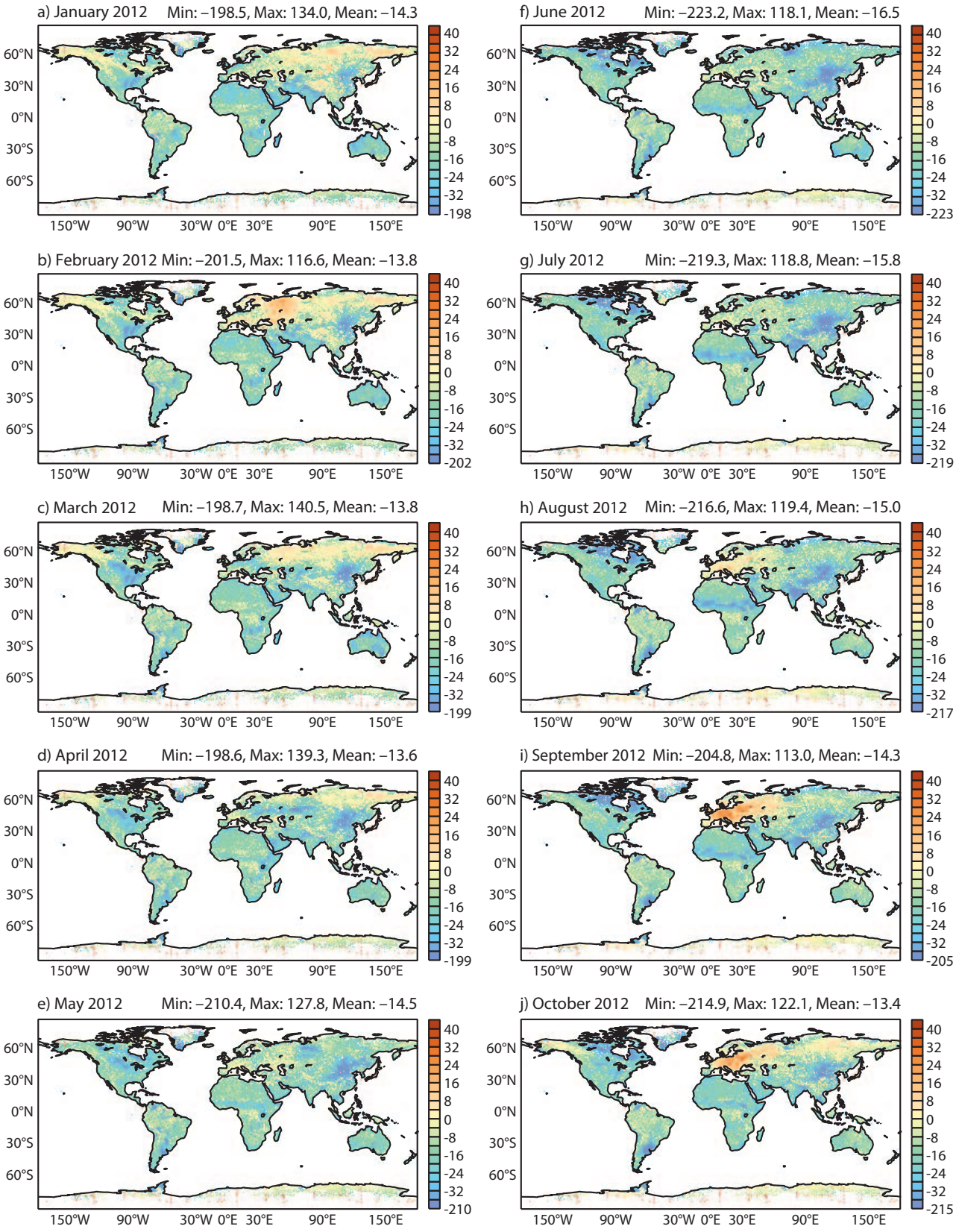

Figure 6: As in Fig. 5, but for YY polarisation.

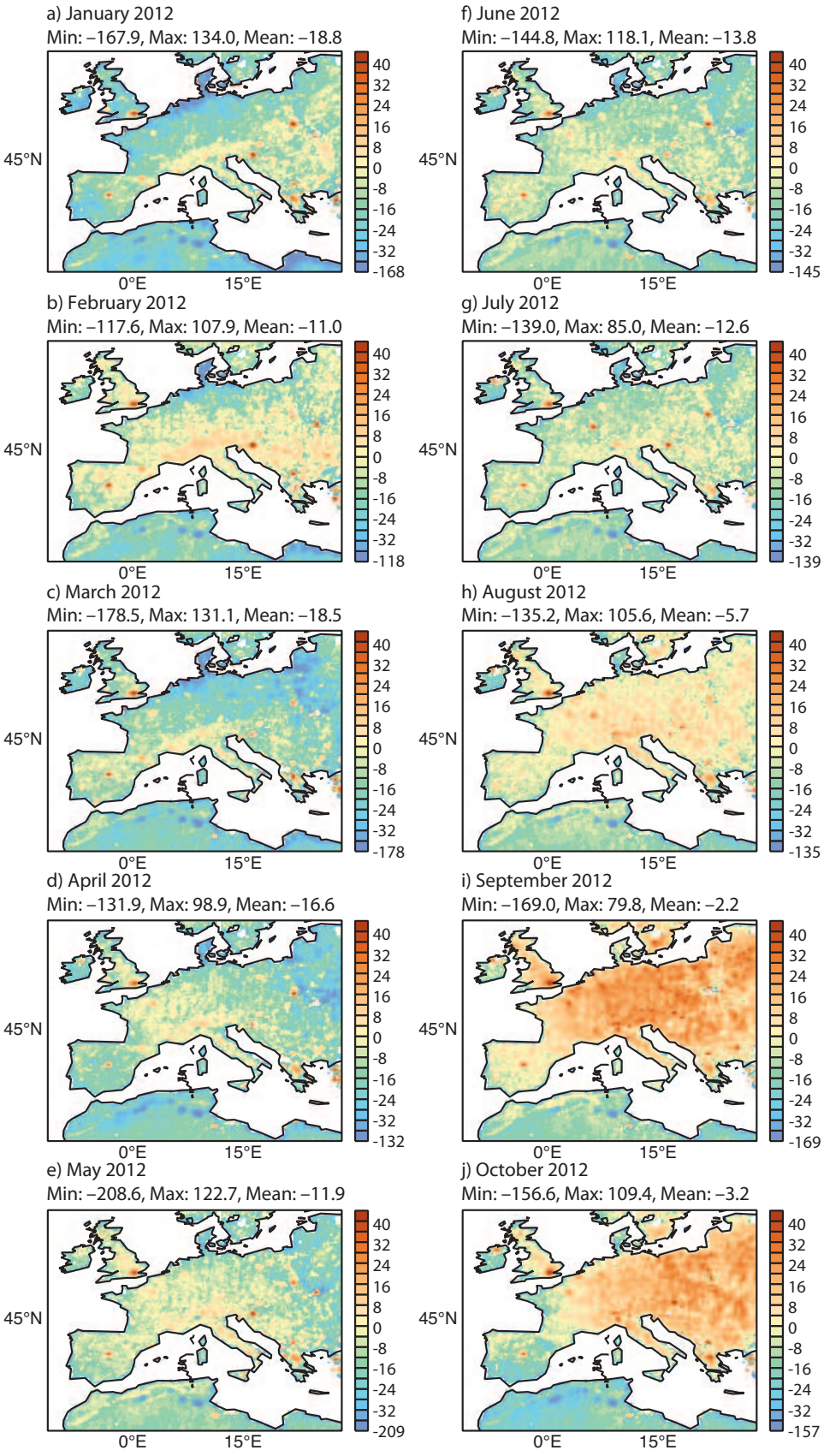

Figure 7: As in Fig. 6, but zoom in over Europe.

3.3 Time series

Figs. 8 to 15 present time series of the observed brightness temperatures, CMEM model equivalents, first guess departures and number of observations, from December 2011 to January 2013. Each value represents one mean value per ECMWF 4DVAR 12 hours assimilation cycle averaged at global scale, hemisphere or continent.

Fig. 8 presents the results obtained at global scale over land pixels. Left panel is for XX polarisation and right panel for YY polarisation. The bias presented in these figures show similar values that those in (10) for 2011. For XX polarisation the annual cycle of bias is dominated by snow and ice covered areas. They can influence the mean bias as much as 10 K. The YY polarisation is less sensitive to snow, and the global mean bias stay quite steady during the whole year. For this polarisation, the model overestimated the observations around 14 K. The bias in the standard deviation show a larger variability for the YY polarisation. This is due to the strongest sensitivity of this polarisation to RFI sources, as it was shown, for example, in Fig. 4 compared to Fig. 3. However, the XX polarisation also shows a larger variability during the snow months at the North Hemisphere.

As it was expected, the bias of the standard deviation are smaller and more stable in the Southern Hemisphere (Fig. 10) than in the Northern Hemisphere (Fig. 9) due to the stronger presence of RFI in the Northern Hemisphere. Compared to 2011, bias of the standard deviation are 2-3 K smaller in 2012 in the South Hemisphere, whereas is not that clear in the North Hemisphere due to the stronger variability of bias. The largest variability is found in Europe (Fig. 11) and Asia (Fig. 12), with values comparable to those of 2011. The XX polarisation also shows a minimum value of bias in Europe and Asia during the summer months, with very little percentage of land covered by snow. For these months the model overestimates the observations. North America (Fig. 13), South America (Fig. 14) and Australia (Fig. 15) show more stable bias. South America, being most of the year free from snow and with little affected by RFI, present a very systematic bias in XX polarisation of -21 K, and -14 K for YY polarisation, whereas the bias of the standard deviation are close to 20 K for both polarisations. Lower values of the bias of the standard deviation, between 18 and 20 K, are found for South America and slightly larger for Australia. The larger variability of bias in Australia (also free from RFI and snow most of the year) is likely due to larger variations of soil moisture. This indicates a potential good area for assimilation.

At the beginning of July a decrease in the number of observations and a larger variability is observed. This issue is under investigation. The larger variability observed in the number of observations in Australia depends logically on the position of the satellite at the time of the acquisition.

In summary, the current CMEM parameterisation used in the current SMOS monitoring suite produces model equivalents which overestimate the SMOS observed brightness temperatures, by around 20 K at 40 degrees incidence angle. An annual bias cycle is observed, stronger for the XX polarisation than for YY polarisation. This cycle is dominated by snow covered areas in the North Hemisphere. Besides, the observations show stronger sensitivity over periods with snow. The largest variability of the bias of the standard deviation in YY polarisation is due to the largest sensitivity to RFI sources. South America is a good example of stable bias, as both of the previous factors (snow and RFI) do not affect the statistics. It is important to note that although for SMOS snow covered areas are interesting for monitoring purposes, observations over snow will not be used for assimilation experiments.

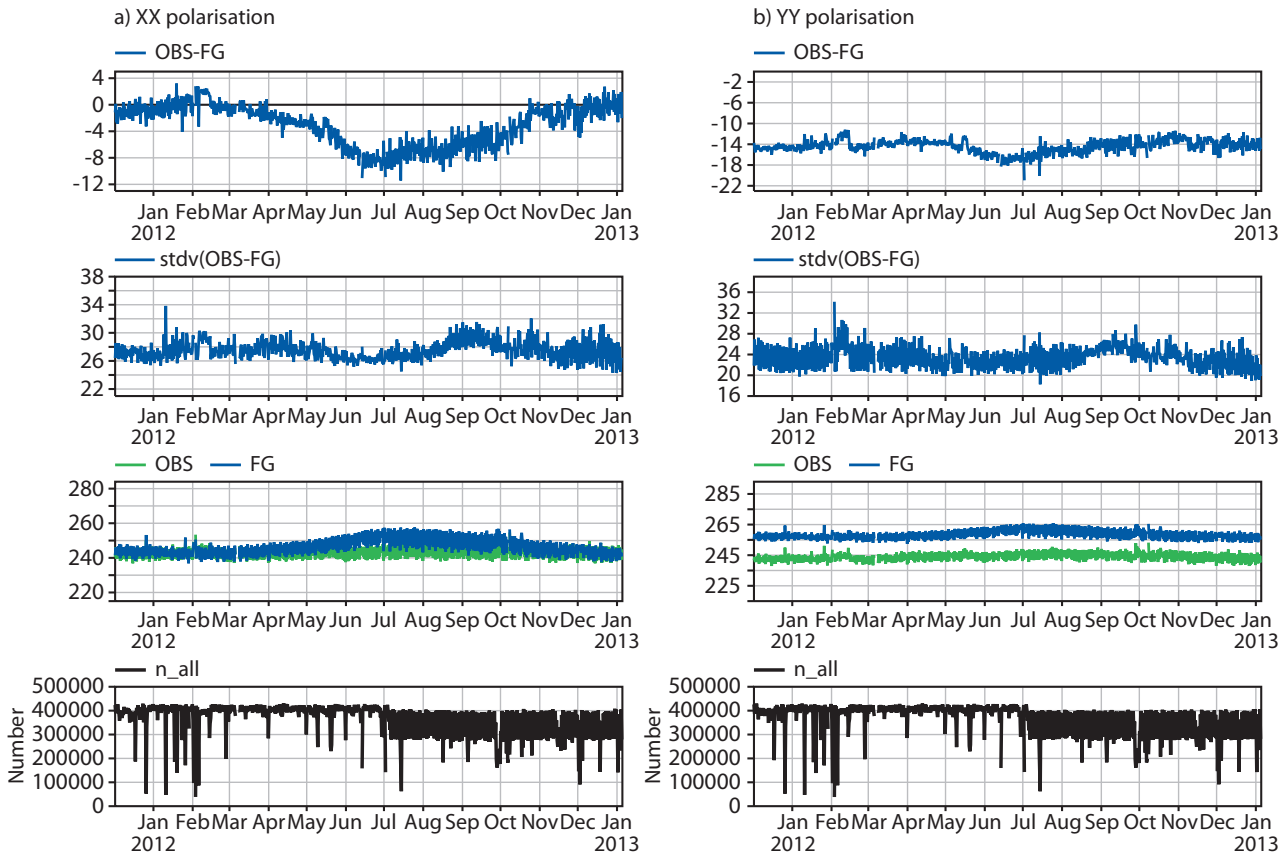

Figure 8: Global scale, time series from December 2011 to January 2013 over continental surfaces, at 40 degrees incidence angle, of mean bias (top figures), mean standard deviation of bias (second top row), comparison between observed brightness temperatures and the CMEM modeled equivalents (third row), and number of observations (bottom figures). Each value is an averaged value per ECMWF 4DVAR 12h cycle. Left panel is for XX polarisation, right panel for YY polarisation.

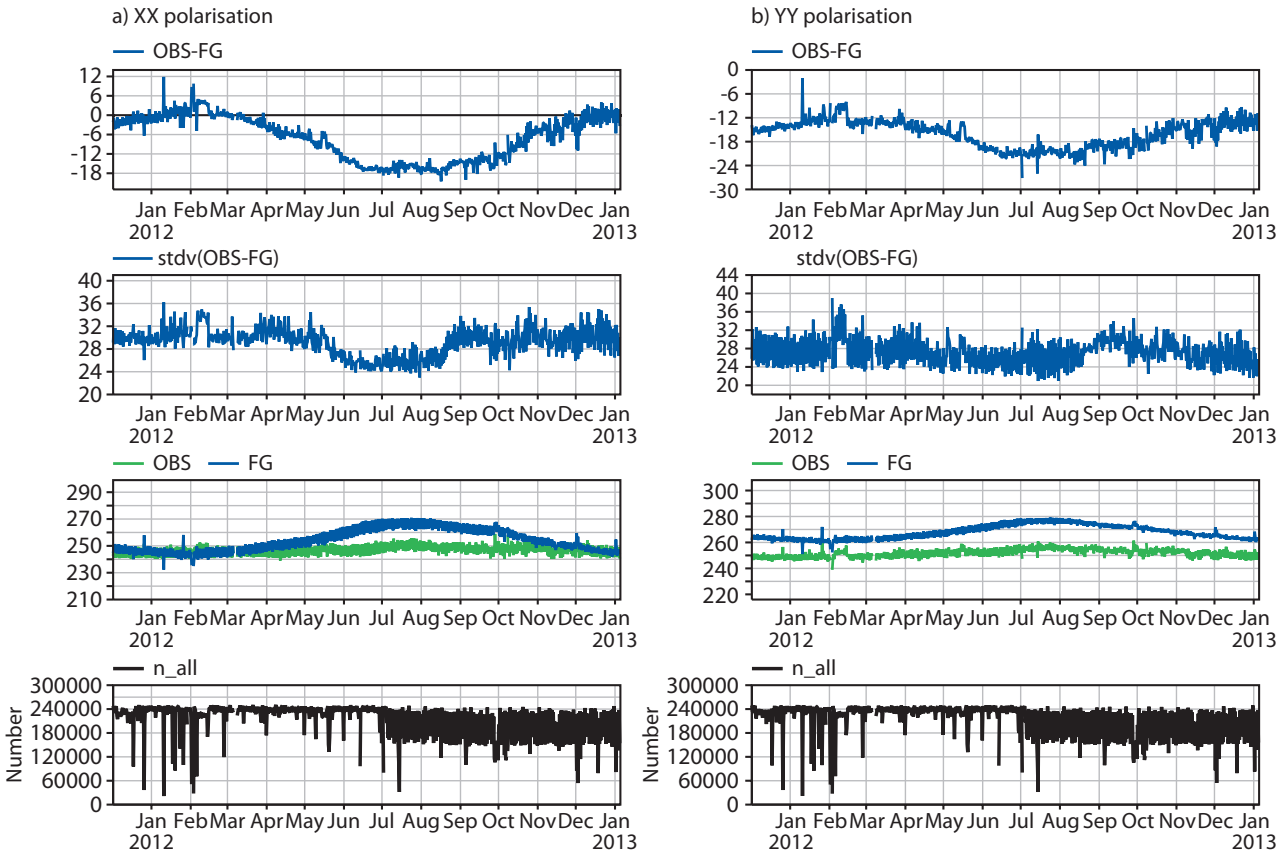

Figure 9: As in Fig. 8 but for the North Hemisphere.

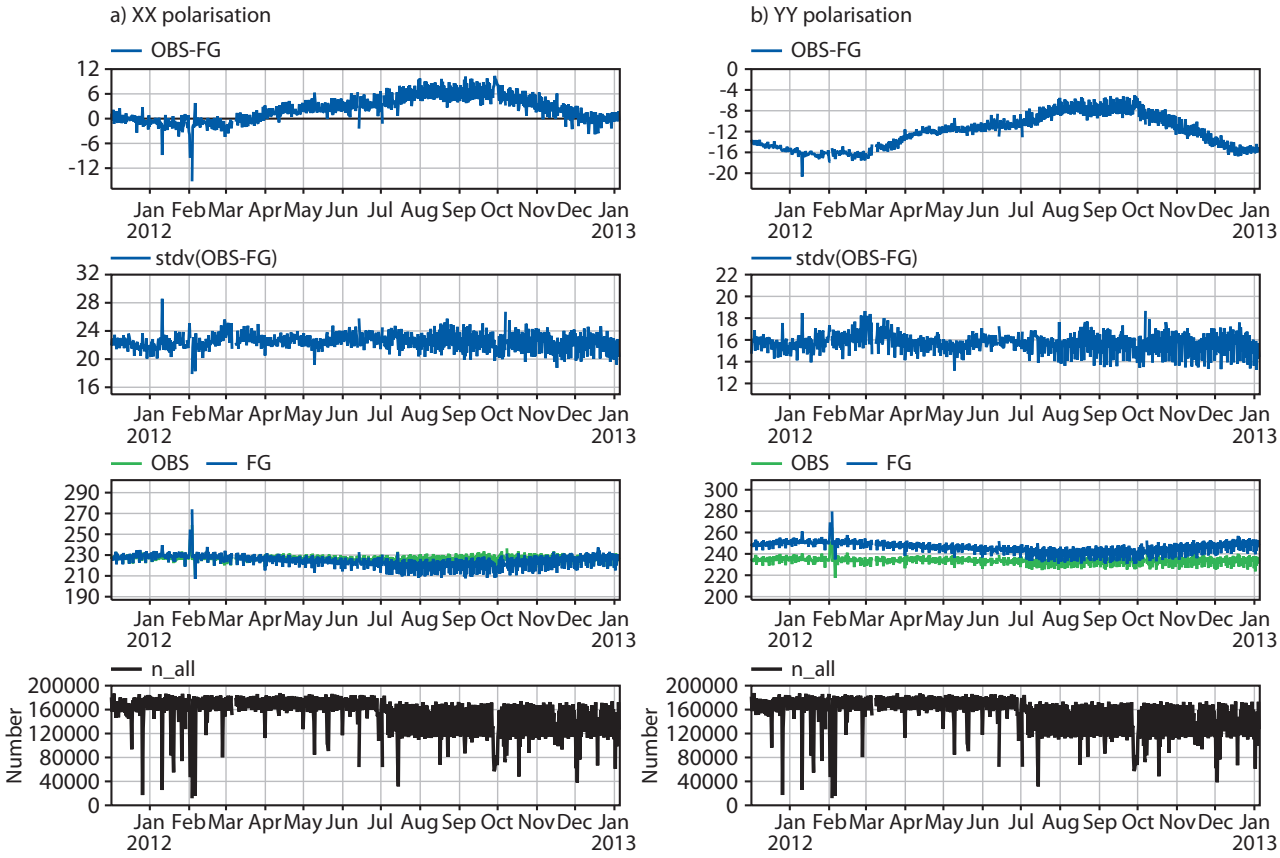

Figure 10: As in Fig. 8 but for the South Hemisphere.

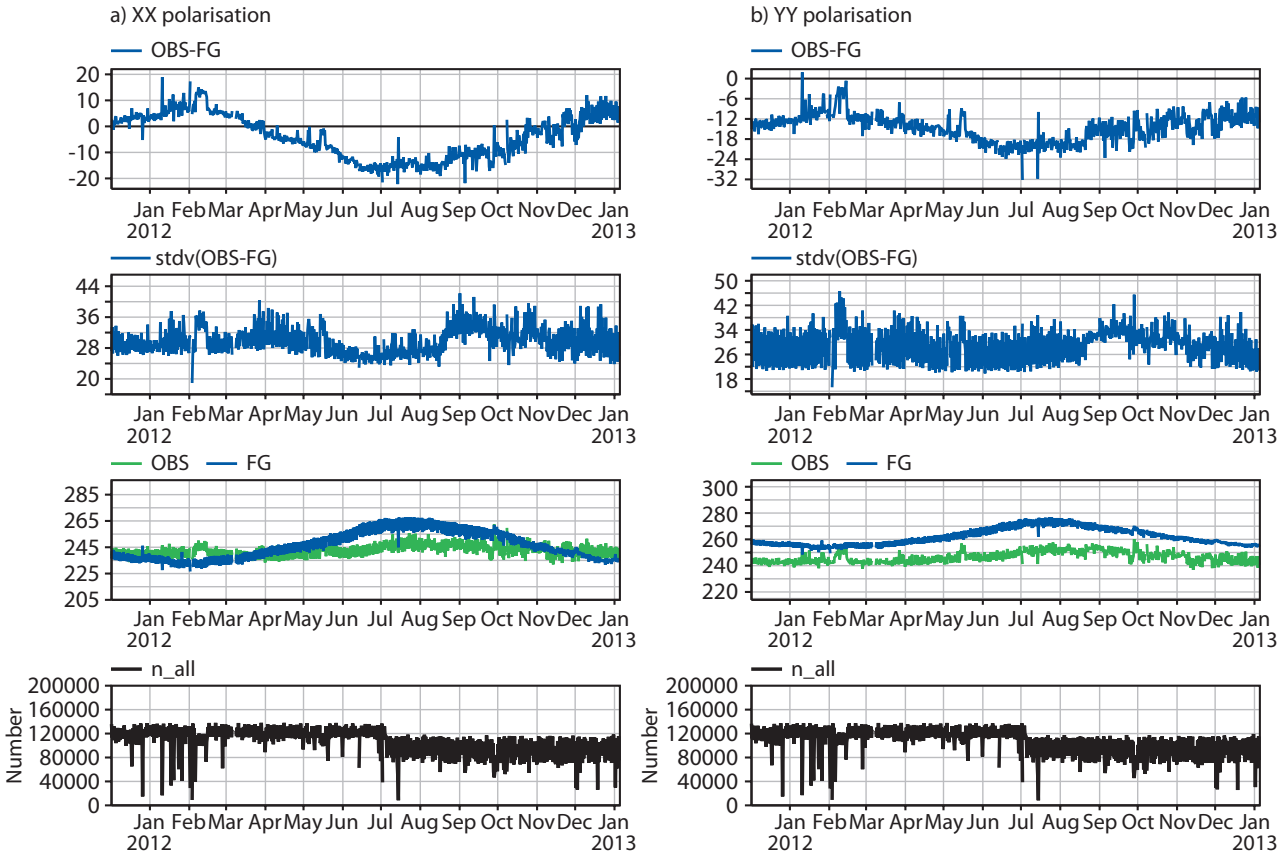

Figure 11: As in Fig. 8 but for Europe.

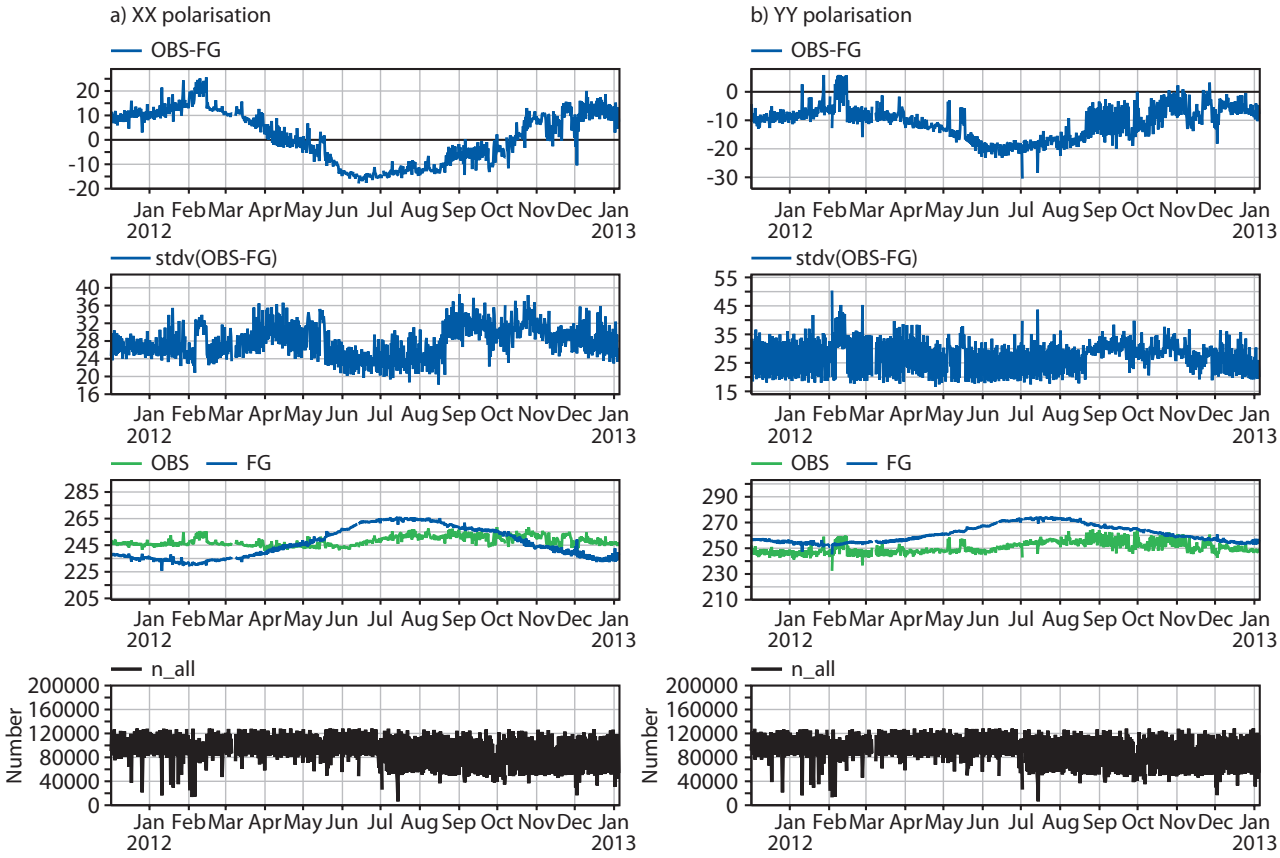

Figure 12: As in Fig. 8 but for Asia.

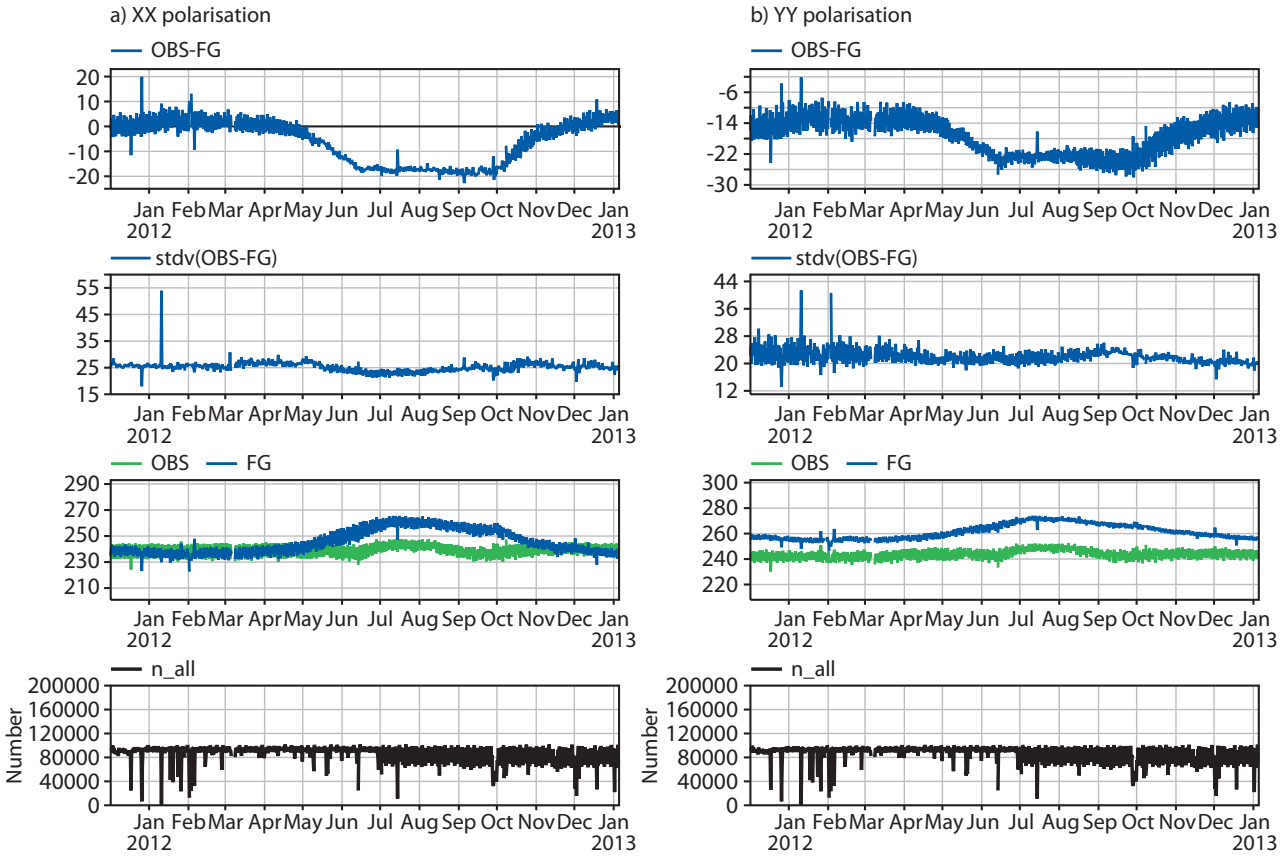

Figure 13: As in Fig. 8 but for North America.

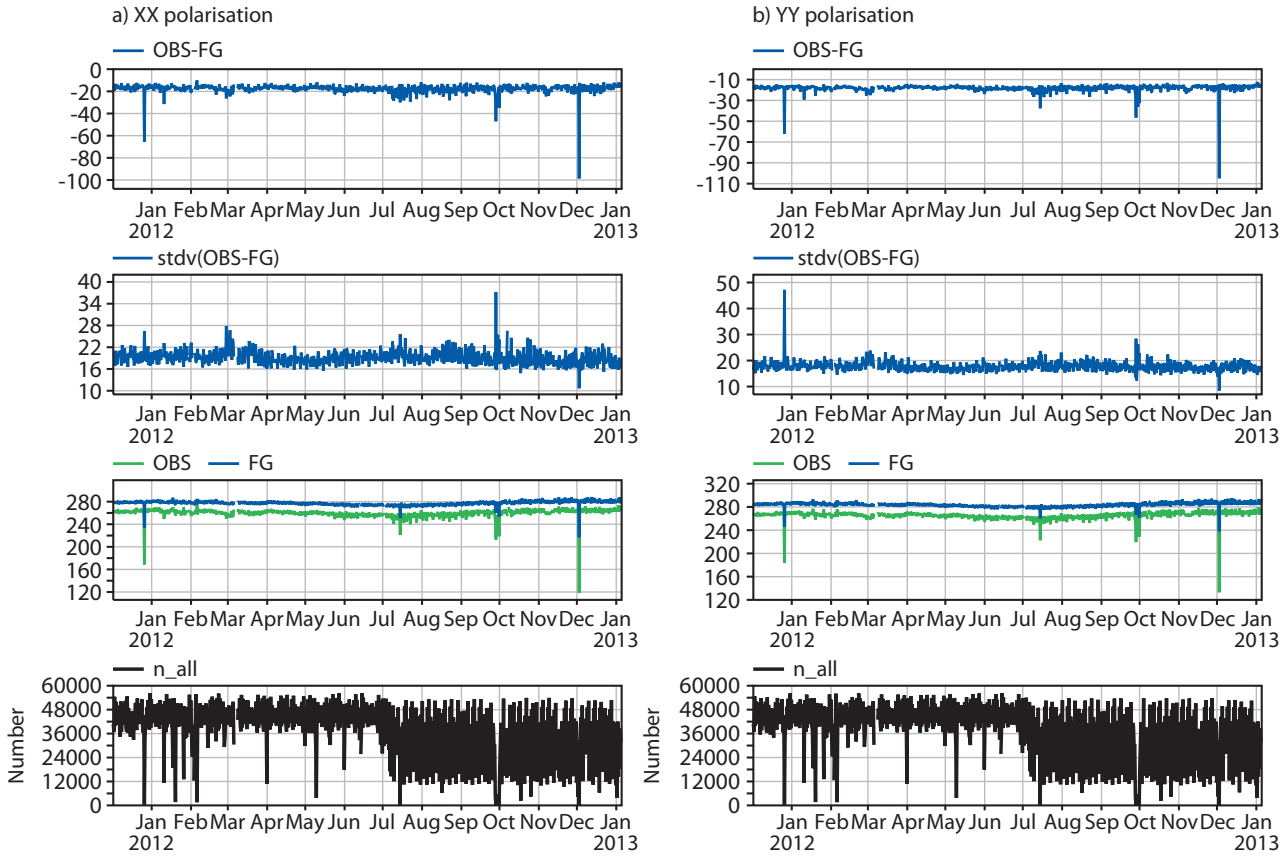

Figure 14: As in Fig. 8 but for South America.

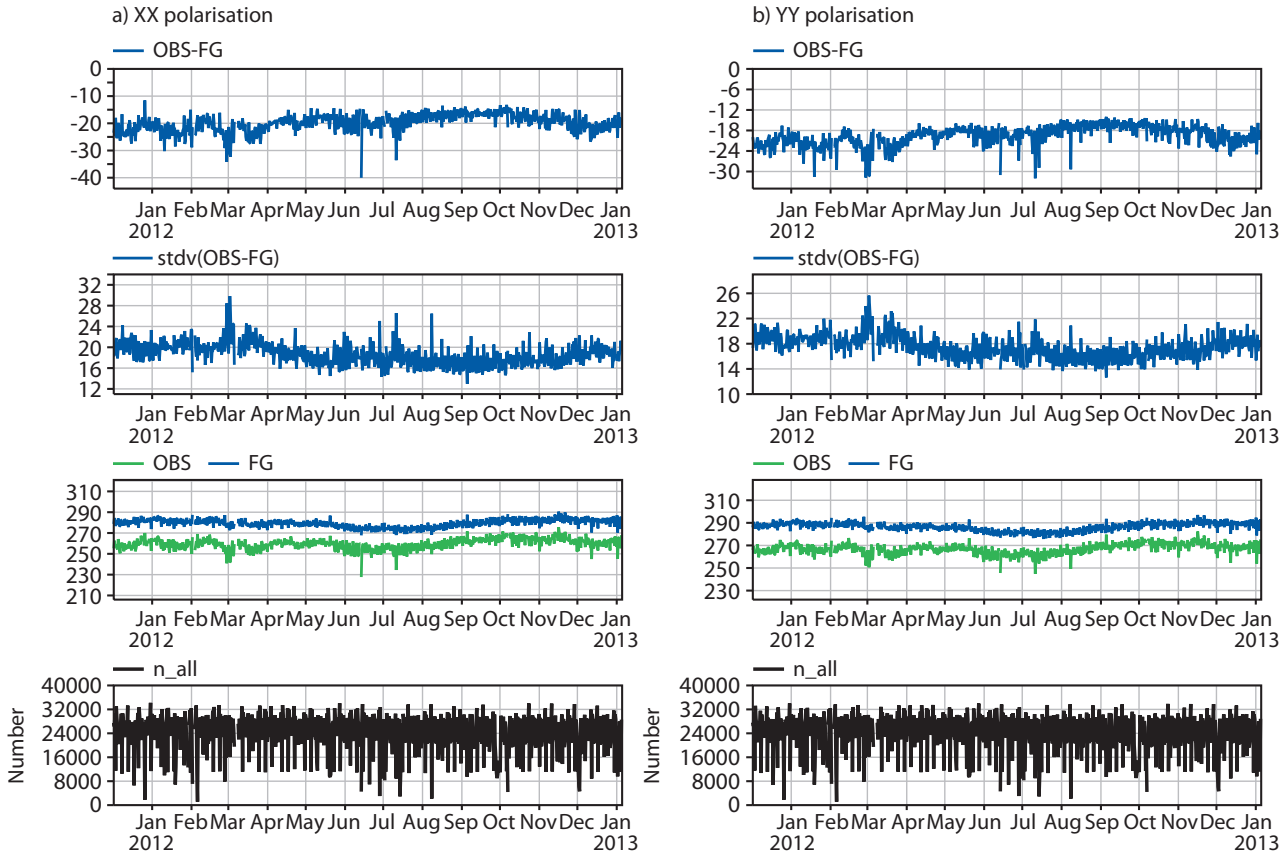

Figure 15: As in Fig. 8 but for Australia.

3.4 Angular distribution of bias

In section 3.3 an analysis of the bias was given at 40 degrees incidence angle. However the results presented can considerably change depending on the viewing angle. The angular distribution of bias product (named as 'scatter plots' in the website) monitors the bias as a function of the incidence angle. This section summarizes the averaged results obtained for the whole year 2012.

Fig. 16 presents the time and spatial averaged bias as a function of the incidence angle, at global scale for the Northern and Southern Hemispheres, and for XX and YY polarisations. Fig. 17 presents the angular distribution of bias for some regions: Europe, North America and Australia. The coloured scale bar refers to the number of observations within each level of bias. It is easily noticeable that the number of observations in Fig. 16 is much larger than in Fig. 17, especially near the zero bias, because the areas over which statistics are computed are much larger. At global scale the number of observations accounted for in these plots is greater than 869 millions, 503 millions for the Northern Hemisphere and 365 millions for the Southern Hemisphere, respectively. This gives an idea on the large number of observations obtained with SMOS, this despite that only observations whose incidence angles are multiples of 10 are included in these plots.

It is shown that, independently of the area shown, the mean bias as a function of the incidence angle for YY polarisation maintain the same distribution. In this case they are maximum at 30 degrees (around -20 K) and minimum at 60 degrees (close to zero). The same values were shown in (10). There are more variability for XX polarisation. The reason is likely the contamination by RFI sources. The South Hemisphere presents more uniform bias per incidence angle, closer to zero, whereas they are larger and grow with the incidence angle in the North Hemisphere. Australia present large bias at 60 degrees for XX polarisation, in average greater than -30 K. Only a few percentage of observations in Australia present positive bias (blue colours in Figs. 17e and 17f). However, bias as large as -90 K can be found here. A good fraction of Australia is covered by deserts and many other pixels have a significant fraction of bare soil. The influence of the soil roughness on the simulated brightness temperatures is especially important here. Likely, the current parameterisation does not account well for the strong variability of soil moisture in this area. With the new coming parameterisation of soil roughness, it is expected to decrease significantly these bias.
These figures also show a significant number of observations with large first-guess departures. These are mainly due to RFI sources, but they are not the only reason as explained in (11).

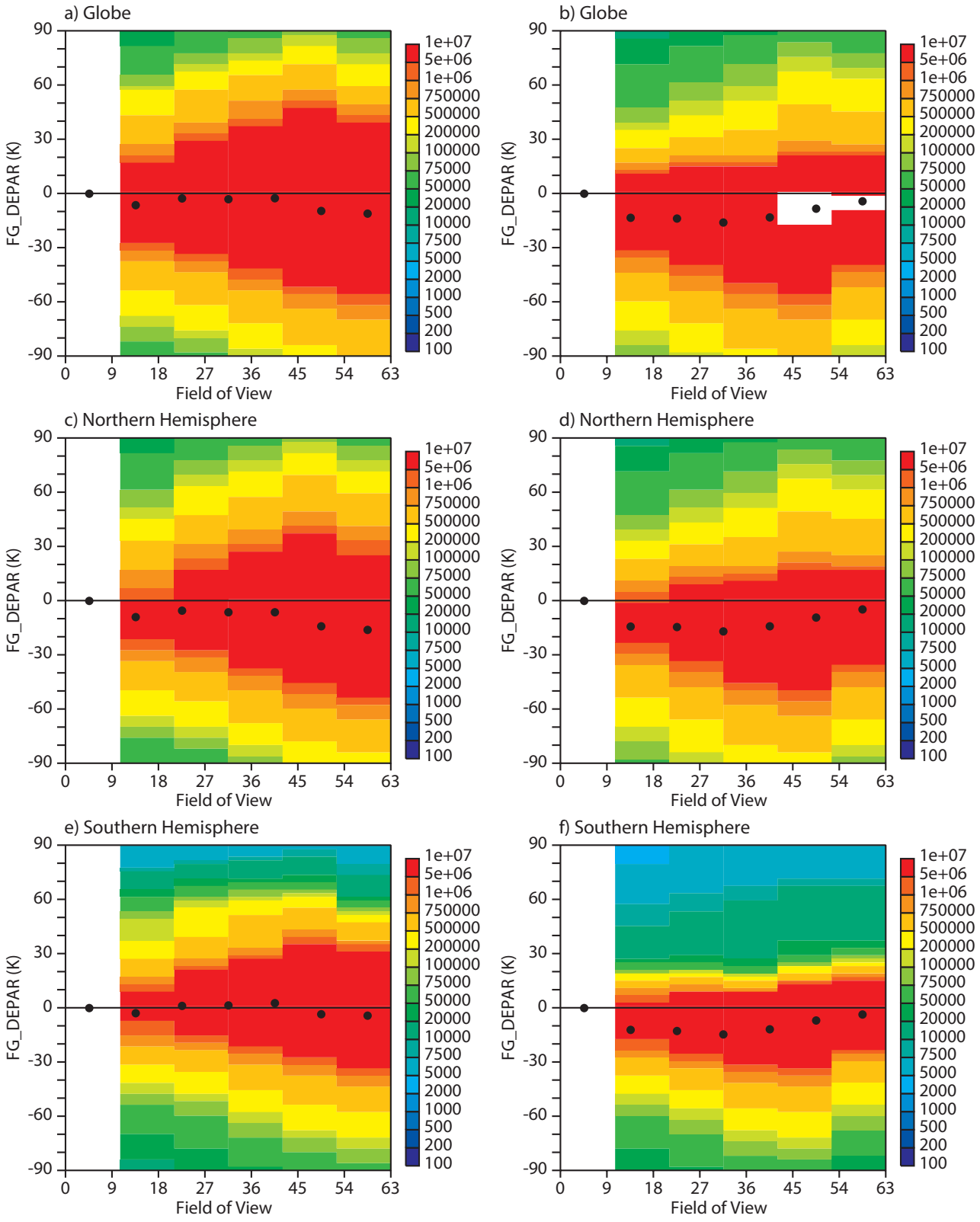

Figure 16: Mean bias as a function of the incidence angle for XX polarisation (left column) and YY polarisation (right column), for the whole year 2012. Only continental surfaces are considered in these figures.

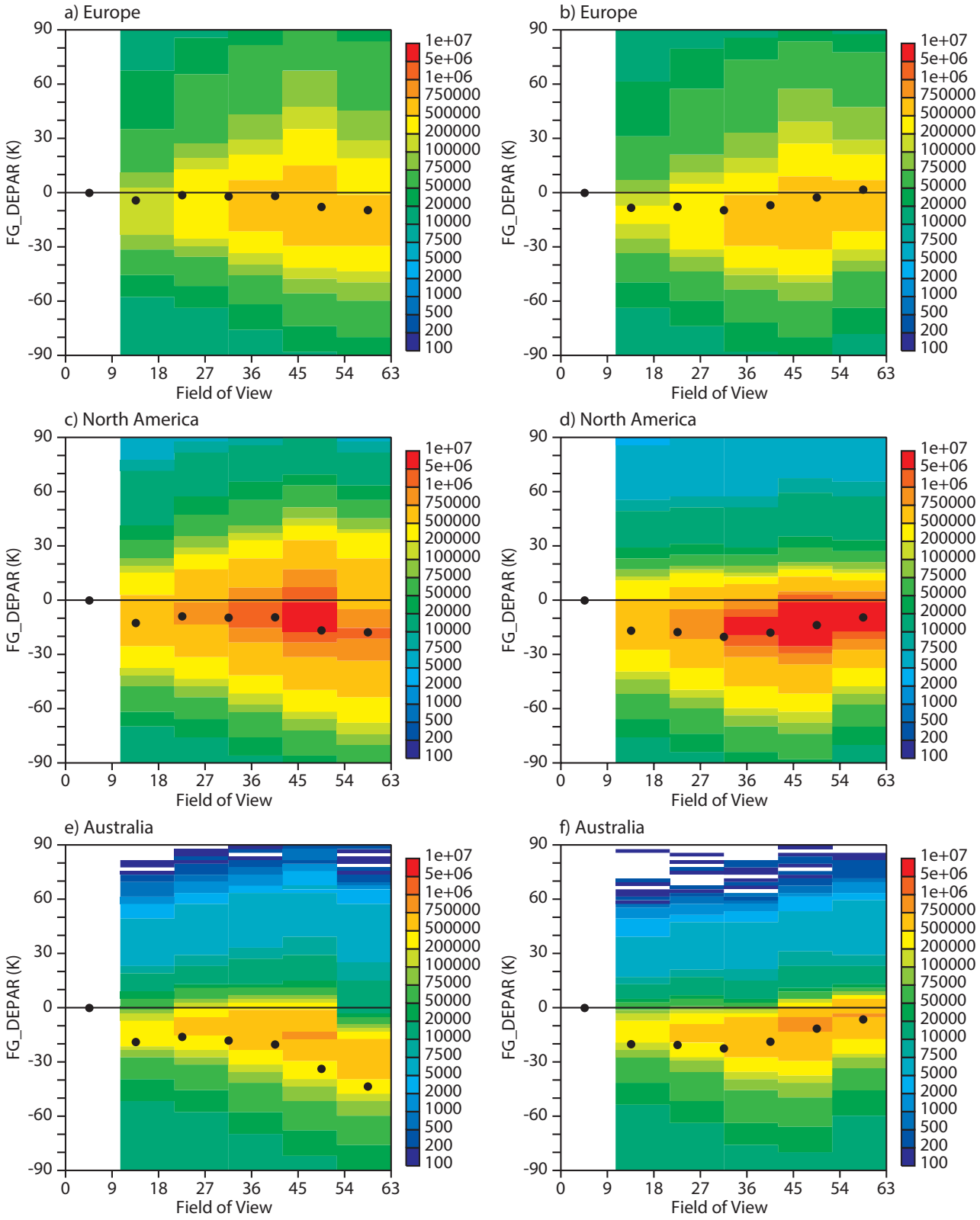

Figure 17: As Fig 16 but for Europe, North America and Australia.

3.5 Hovmöller plots

Hovmöller plots provide a latitudinal-temporal perspective of a statistical variable. In the plots of this section, each point represents a 12h average per 2.5 degrees of latitude. They make it possible to study the seasonal evolution of the statistical variables under study per bands of latitude, and therefore they are very complementary of the time-averaged geographical mean fields and time series. Punctual problems in the data that could be unnoticed in time-averaged geographical plots can be easy identified in these plots.

In Fig. 18 the Hovmöller plots of the observed brightness temperatures are shown for the period from December 2011 to January 2013, for six incidence angles. They clearly show the seasonality of brightness temperatures for both polarisations, increasing towards the Northern Hemisphere, from May until August, and increasing in the Southern Hemisphere the rest of the year. This is especially visible at 60 degrees incidence angle. Maximum values are obtained at tropical latitudes. A strong difference is observed in the mean brightness temperatures between 20 and 60 degrees incidence angles, with a mean difference for both polarisations of more than 15 K. These values are equivalent to those shown for 2011.

First-guess departures are presented in Fig. 19, for the XX polarisation. They are very well correlated with snow covered areas for this polarisation, as the emission over snow is currently strongly underestimated, so large departures are obtained in these areas. It is observed that the maximum of snow cover is obtained in February in the North Hemisphere, with snow down to a latitude of approximately 35 degrees North. The Antartic region is also clearly seen in these figures, as presenting the same signature that the snow covered areas in the North Hemisphere (a likely underestimation of the soil emission). In general, the departures in the Equator are quite low, as the representation of dense vegetated canopies is quite accurate and the annual dynamic small. The white line observed around 60 degrees South is due to the absence of land points. The averaged values of first-guess departures are very similar to those of 2011, with differences reflecting the different distribution of soil geophysical variables (soil moisture, soil temperature) during the years 2011 and 2012.

Fig. 20 shows the standard deviation of the first-guess departures, for three different incidence angles. The red, non uniform band observed between 20 and 60 degrees North latitude reflects excessive variability of the first-guess departures and is mainly due to the contamination produced by intermittent sources of RFI. However, they are not the only reason. The presence of snow and ice contributes too. This was shown in the time series plots (section 3.3), where larger variability of the observed brightness temperatures was observed over snow and ice covered areas. For example, in XX polarisation a slight reduction of the variability of first-guess departures is observed for all incidence angles during summer months in the North Hemisphere (a more pale red). This effect is less visible in YY polarisation, less sensitive to snow and ice.

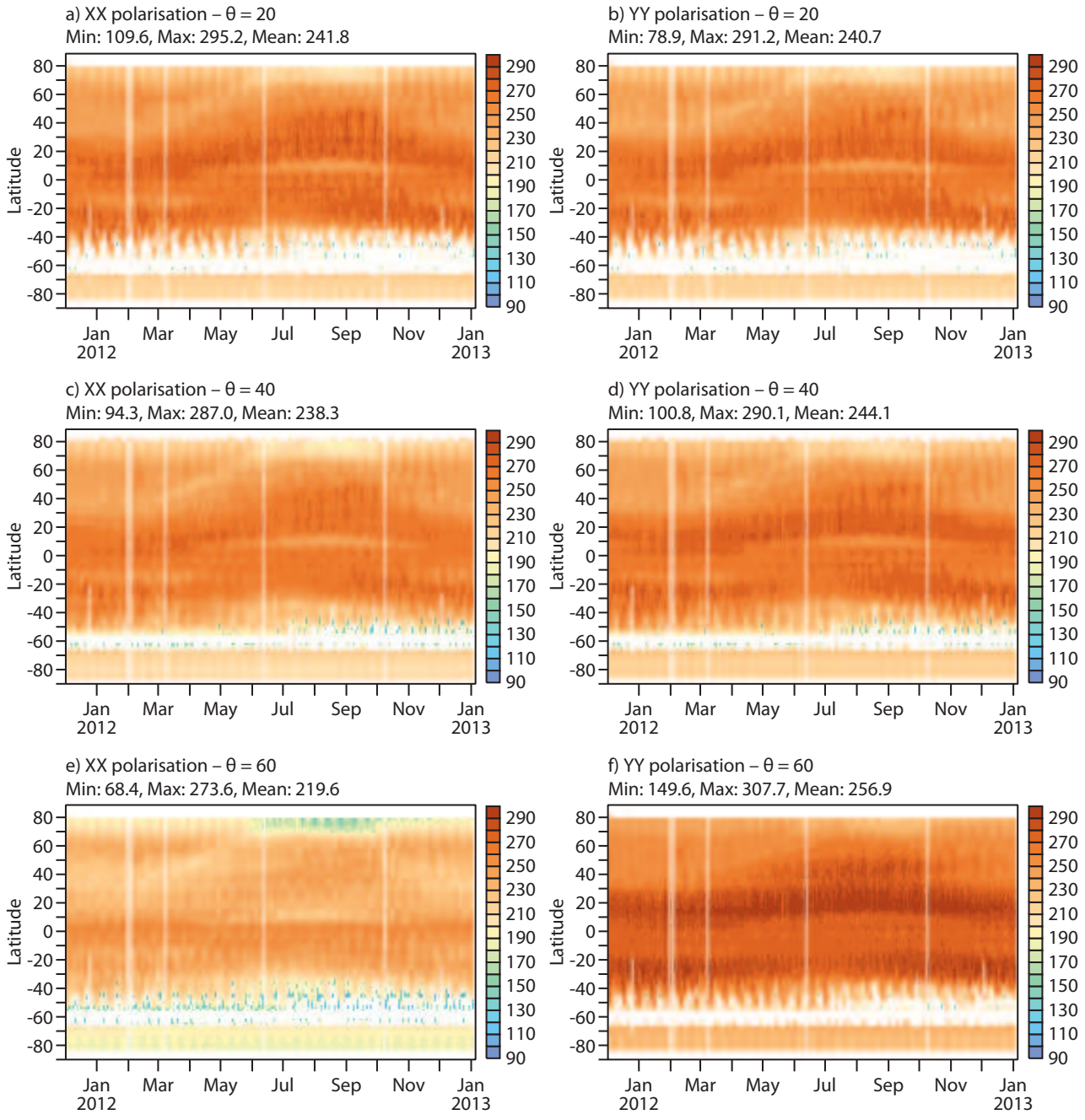

Figure 18: Mean SMOS observed brightness temperatures per bands of 2.5 degrees of latitude as a function of time. Left panel if for XX polarisation and right panel for YY polarisation. Figures are shown for 20, 40 and 60 degrees incidence angle.

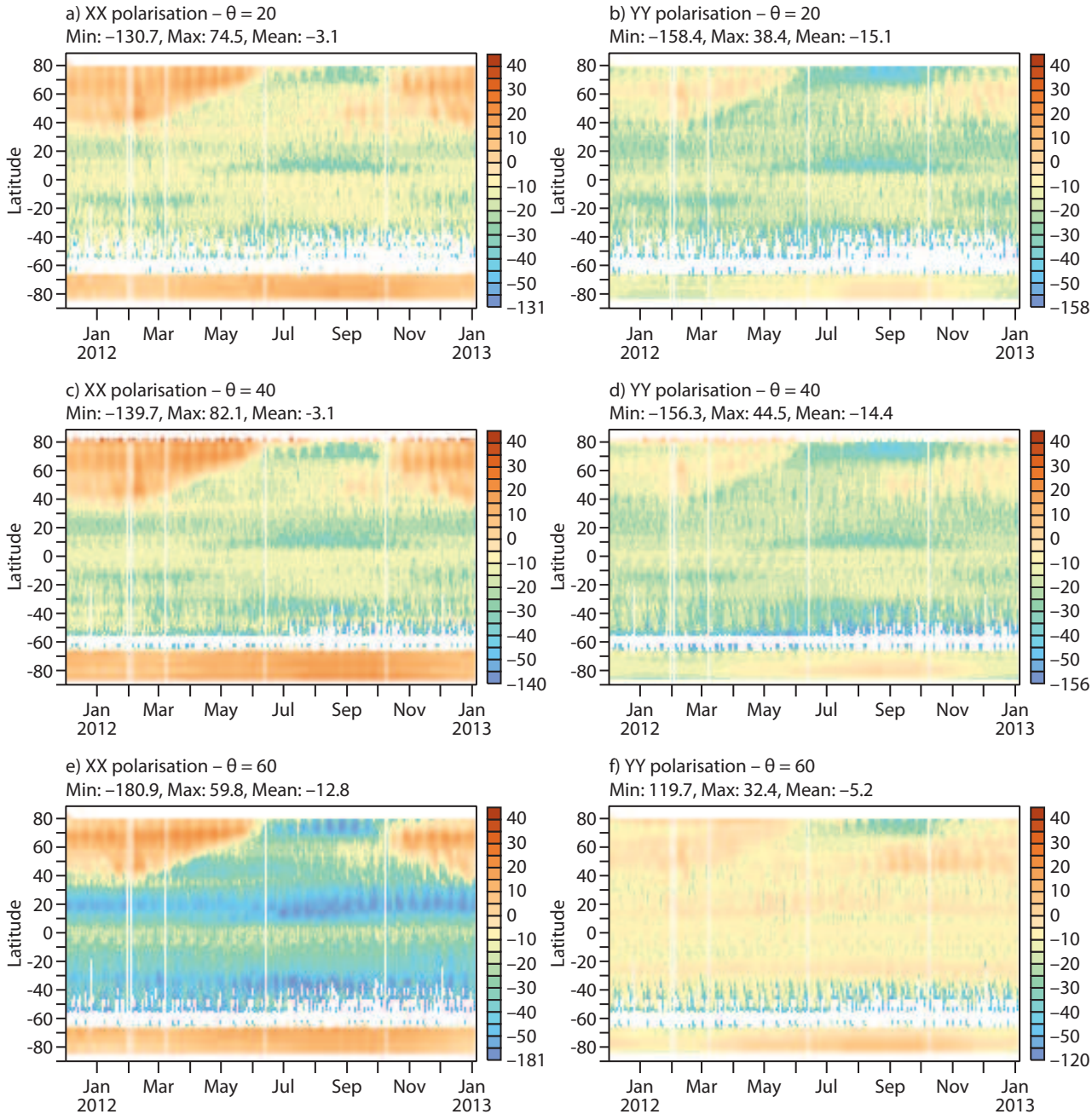

Figure 19: As in Fig. 18, but the variable shown is the first-guess departures.

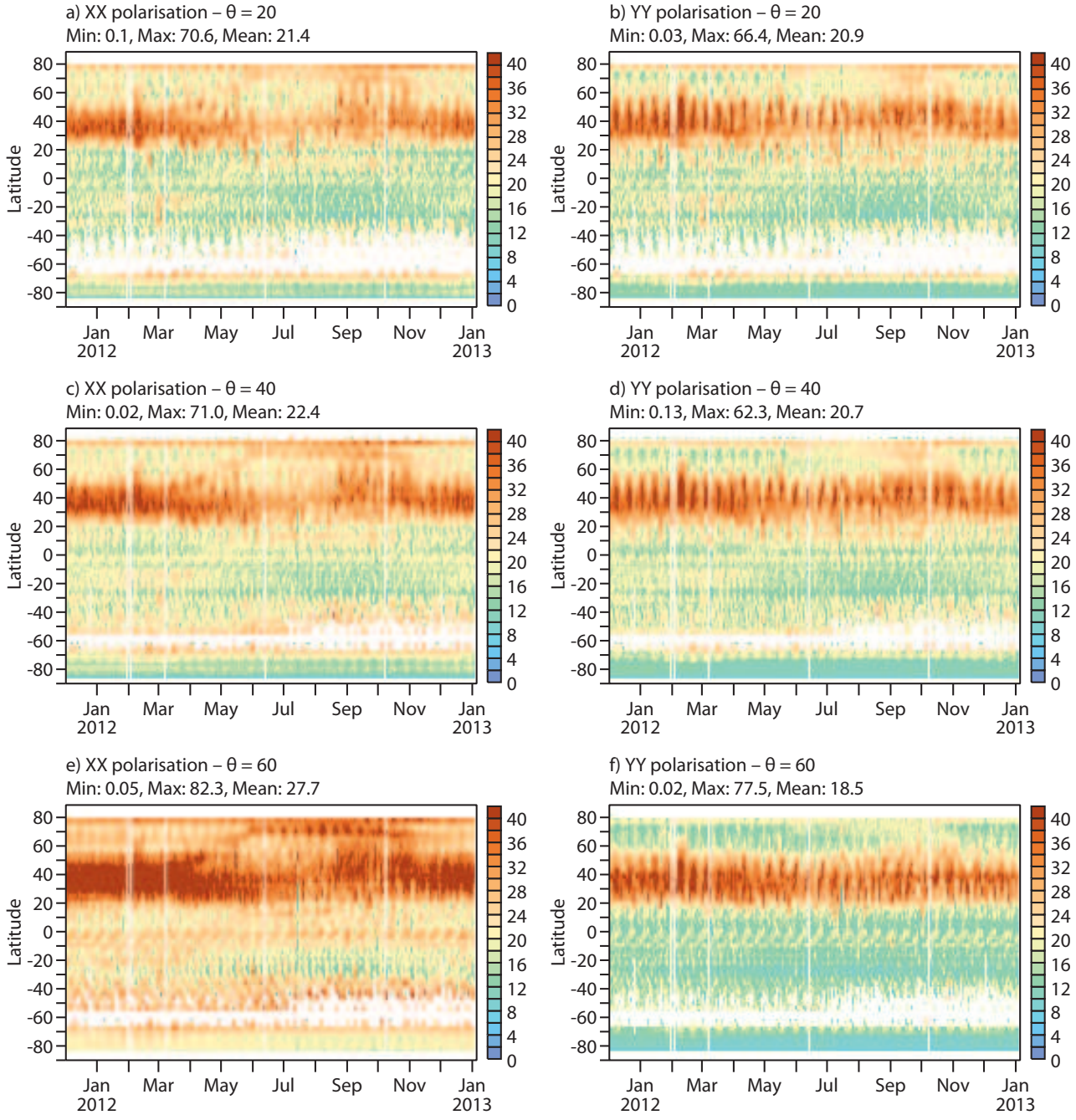

Figure 20: As in Fig. 18, but the variable shown is the first-guess departures standard deviation.

4 Monitoring over oceans

In this section some of the more relevant results obtained with the monitoring suite [see a description in part III of (12) and (11)] over oceans are presented. In (10) a substantial description of the statistical variables obtained over oceans in 2011 was given, including time-averages geographical mean fields, time series and Hovmöller plots. However, there it was pinpointed that with the current parameterisation used in CMEM, the effect of the wind and of the galactic noise in the L-band emission over oceans was not accounted for. On the contrary, it considers the ocean as a smooth surface of water. Since these two missing components are important for oceans, in this report only statistics involving the observed brightness temperatures are presented. Otherwise, any conclusion using the model simulation would lack of solidity.

4.1 Time-averaged geographical mean fields.

Fig. 21 and Fig. 22 show the averaged brightness temperatures over ocean surfaces as a function of the incidence angle for July 2012 and XX polarisation (Fig. 21) and YY polarisation (Fig. 22). Each value represents a mean value in boxes of 0.25 degrees. As it occurs over continental surfaces, brightness temperatures decrease with the incidence angle for XX polarisation and increase for YY polarisation. However the dielectric constant of water is very different of that of soil, and therefore water and soils have very different emissivity in the L-band. Lower values of brightness temperatures are found over oceans compared to land surfaces, on average 120 K lower for July 2012 at 50 degrees incidence angle. The YY polarisation has a larger angular dynamical range, of about 30 K larger in average than the XX polarisation between 20 and 60 degrees. These values are very consistent with those of 2011. The frozen Antarctica can be clearly observed in these figures, as the emissivity over a frozen surface is much larger, and therefore the observed brightness temperatures. The observed brightness temperatures in the North Pole are also significantly larger, given that even in summer still larger areas are covered by ice or snow. Brightness temperatures over oceans have a much lower dynamical range, as they are relatively homogeneous in comparison to land surfaces. These figures also show clearly the inland water bodies (mainly lakes), especially clear the extended areas of lakes in Finland and Canada.

The evolution of the SMOS observed brightness temperatures standard deviation in the XX polarisation at 40 degrees incidence angle, from January to October 2012 (one averaged value per month), is shown in Fig. 23. Fig. 24 is the equivalent figure for YY polarisation. The spatial resolution is 0.25 degrees. The spatial monthly average of brightness temperatures standard deviation shows similar values than for 2011, slightly lower for some months. As it happened for 2011, near China, Middle East and Eastern European coastlines the standard deviation of brightness temperatures is very large, which is due to RFI. The contamination is not only limited to coastlines, but in same cases several hundred of kilometers offshore. The main anomaly is observed in February 2012. During this month abnormal large variability of the observed brightness temperatures is found mainly around the coasts of Europe. In February 2012 a persistent DPGS FTP malfunctioning occured. This affected the number of observations delivered in NRT and it could be the cause or a contribution to these abnormal values. The other raison might be a strong source of RFI in Europe during this month. However, the previous problems of RFI reported in Poland during summer 2012 are not reflected in larger contamination over seas.

As it was also reported in (10), the transition zone between frozen and liquid water over Antarctica is clearly observed in Figs. 23 and Fig. 24. This is due to the very different dielectric properties of frozen and liquid water, and therefore presenting very different emissivities. As this is a very sensitive and dynamical zone, the variability of brightness temperatures is very large. During the summer months at the Southern Hemisphere this transition zone can barely be observed, or at least is very close to the Antarctica continent, whereas it moves far from the coastline during the winter months.

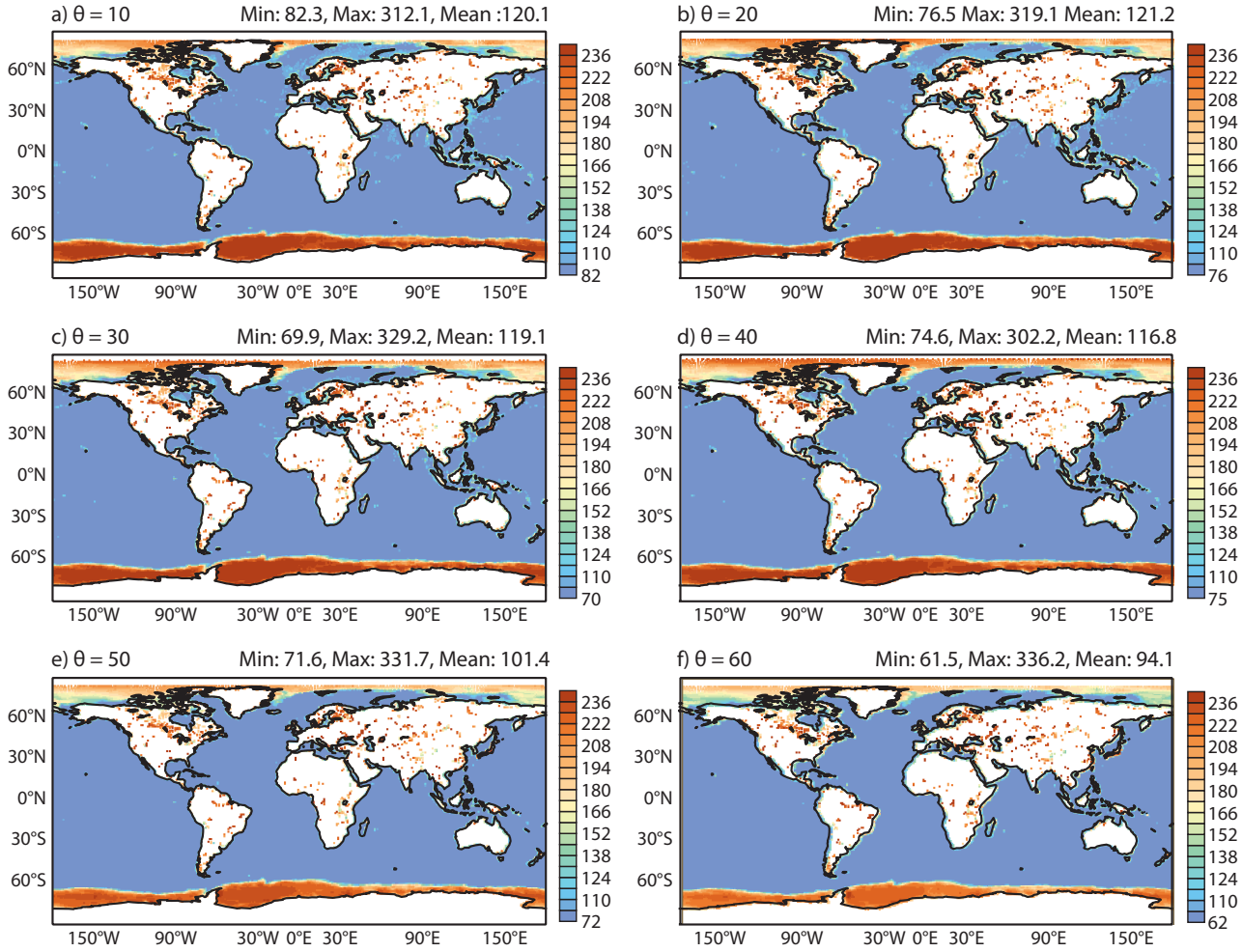

Figure 21: July 2012, angular global mean of the SMOS observed brightness temperatures for ocean surfaces and for XX polarisation. Each value represents a mean value of all the data inside a box of 0.25 degrees.

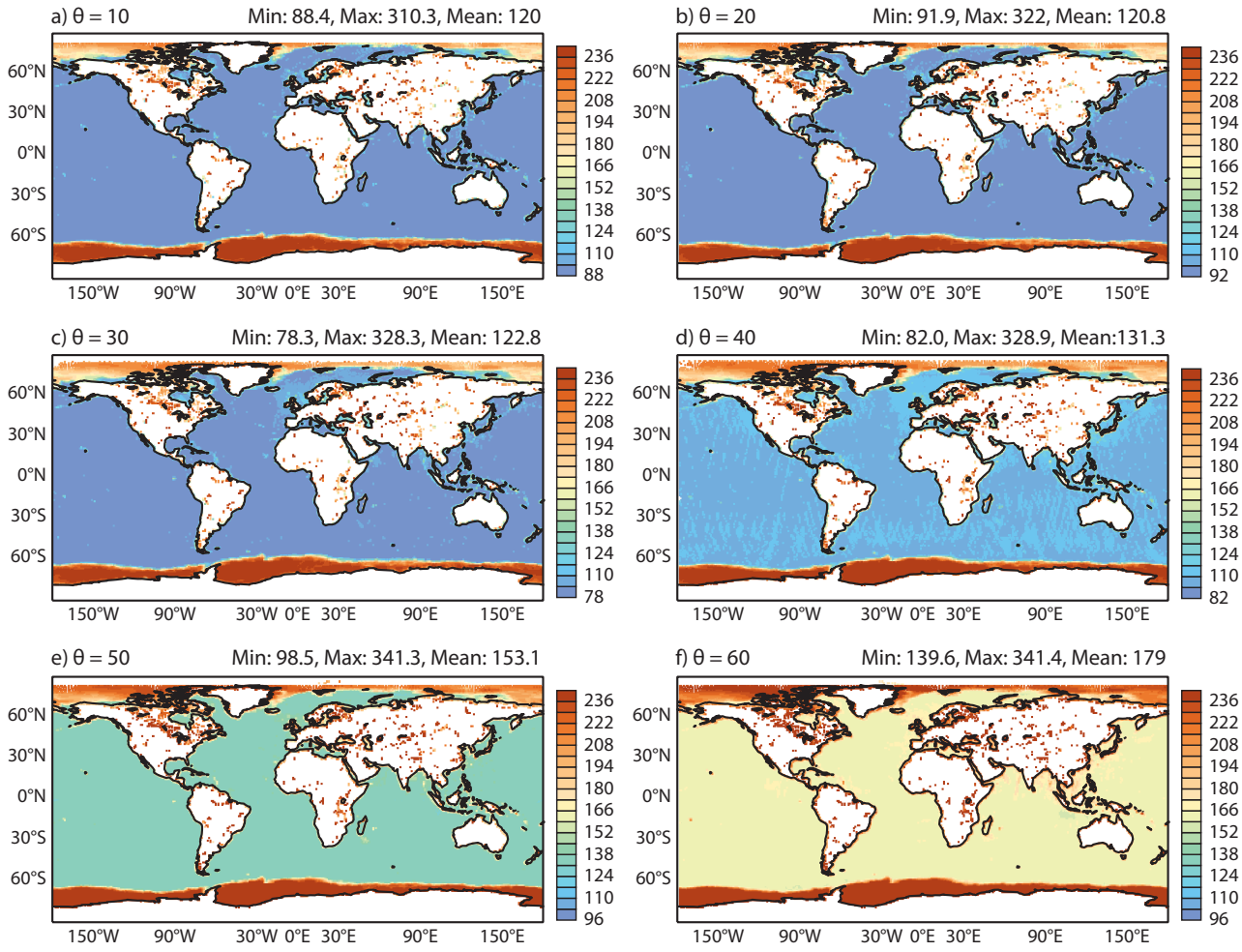

Figure 22: As in Fig. 21 but for YY polarisation.

4.2 Hovmöller plots

Fig. 25 show the latitudinal-temporal evolution of the observed brightness temperatures, averaged per bands of 2.5 degrees of latitude from November 2011 to November 2012. They are produced at 20, 40 and 60 degrees incidence angle and for XX and YY polarisations. The evolution of the fraction of frozen sea around the poles can be clearly followed as they present constrasting larger brightness temperatures than the rest of the seas. They are maximum between March and April 2012 at the North Hemisphere, coinciding with the minimum in the South Hemisphere. Brightness temperatures clearly decrease with the incidence angle for XX polarisation, while comparatively they increase faster for YY polarisation.

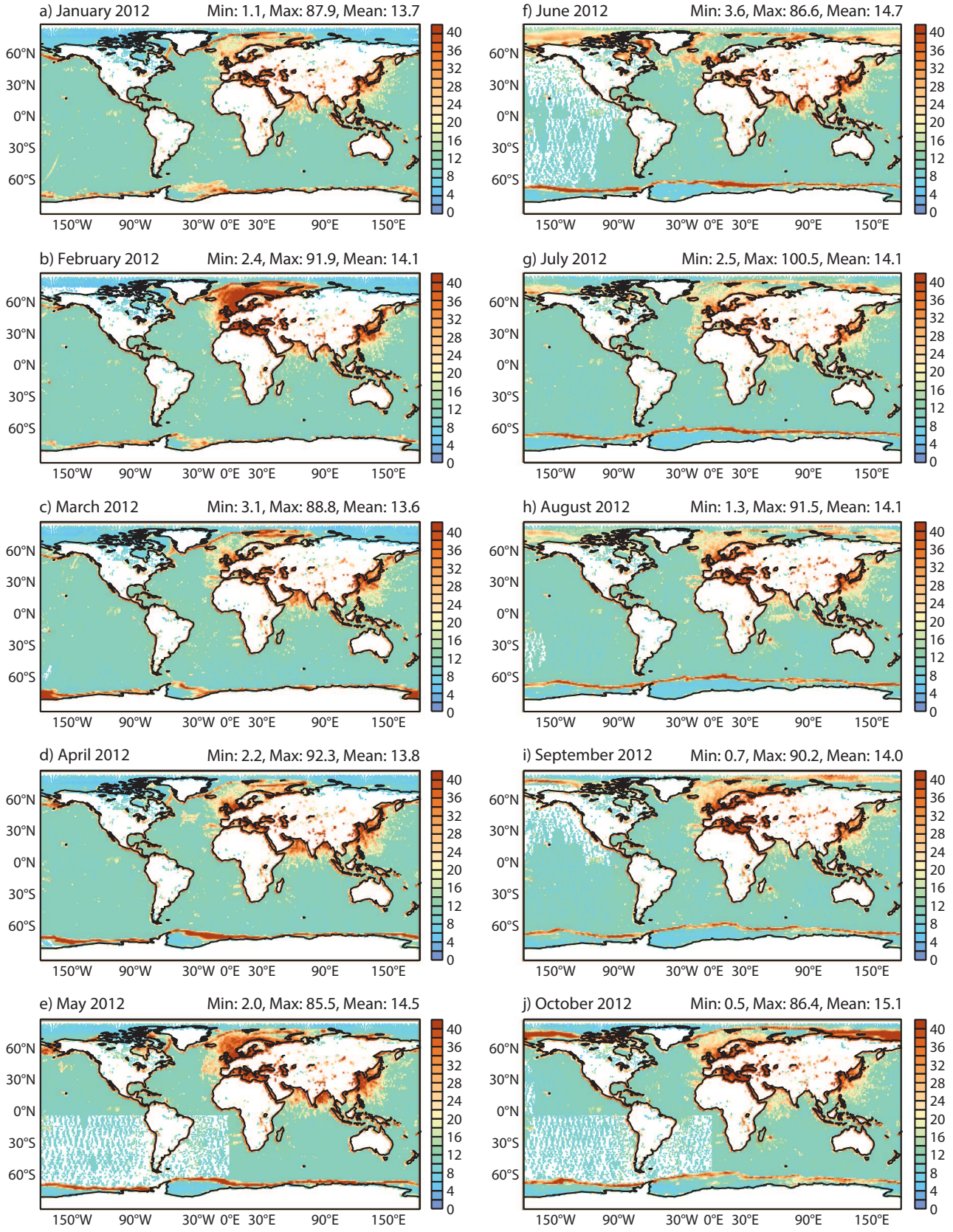

Figure 23: Monthly mean of the SMOS observed brightness temperatures standard deviation, for XX polarisation and for ocean surfaces only. Each value represents a mean value of all the data inside a box of 0.25 degrees. The incidence angle is 40 degrees.

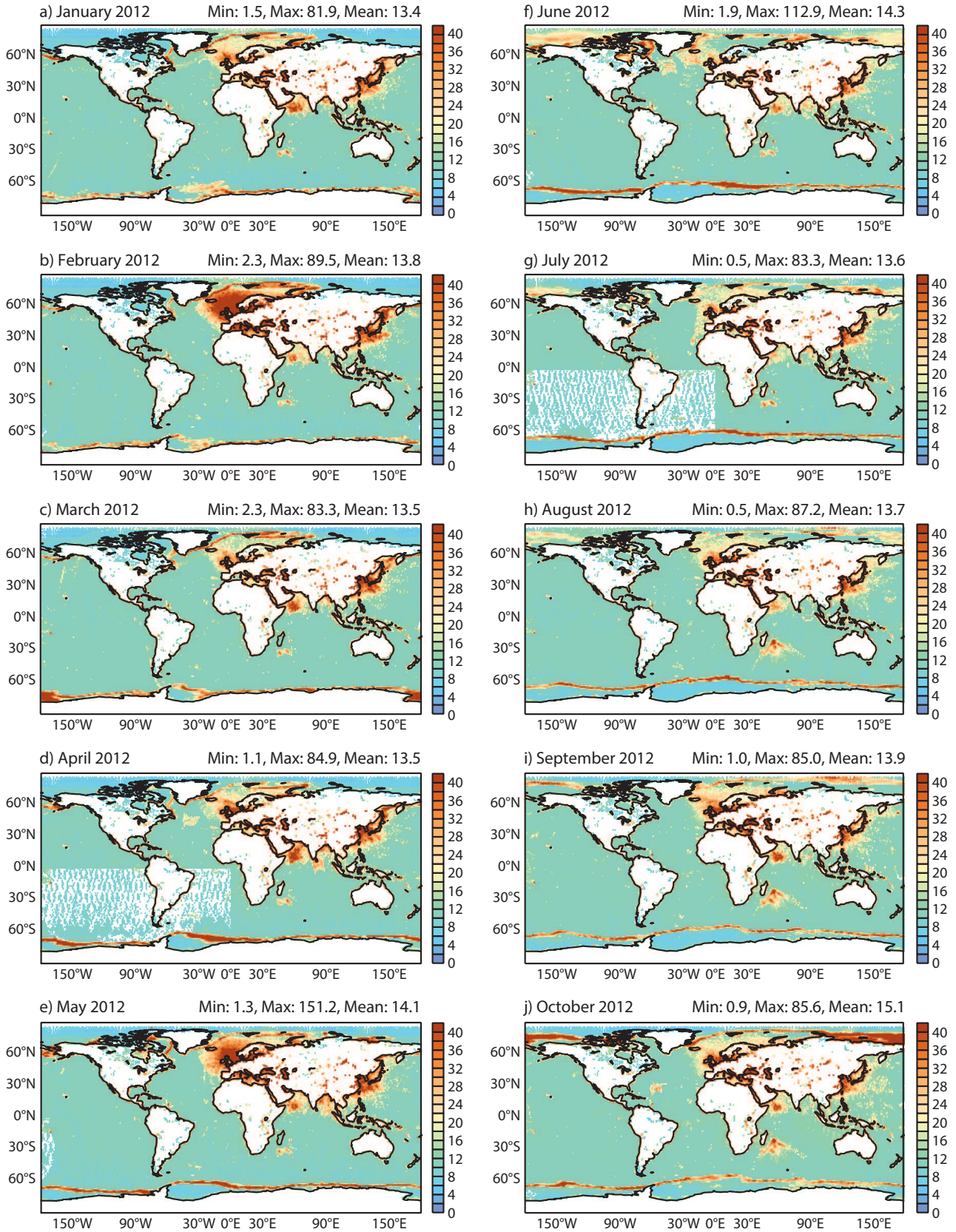

Figure 24: As Fig. 23 but for YY polarisation.

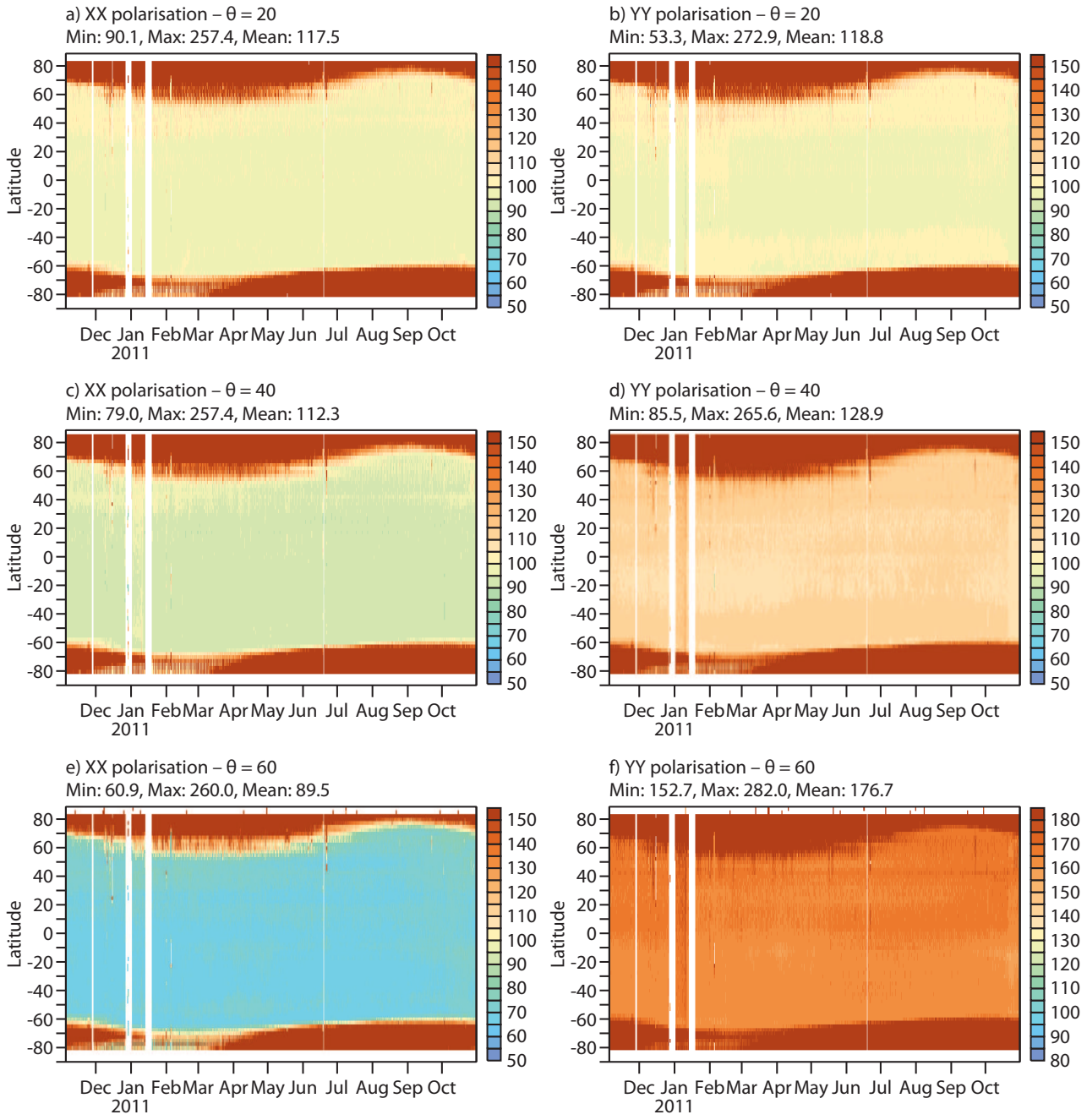

Figure 25: Mean SMOS observed brightness temperatures per bands of 2.5 degrees of latitude as a function of time, only over oceans. Left panel if for XX polarisation and right panel for YY polarisation. Figures are shown for 20, 40 and 60 degrees incidence angle.

5 Summary

This is the third SMOS monitoring report. It present some of the statistics obtained with the Near Real Time SMOS monitoring suite for the year 2012. The ECMWF passive microwaves emission model CMEM is used to simulate brightness temperatures at the top of the atmosphere. Geolocated SMOS observed brightness temperatures are compared to CMEM values at the satellite antenna reference frame and in NRT. A whole annual cycle of statistical variables was computed and analysed.

Observed brightness temperatures behave as expected, i.e, they decrease with the incidence angle for XX polarisation and they increase for YY polarisation. However, the dynamical amplitude of brightness temperature with the incidence angle is greater for XX polarisation over lands, indicating a larger sensitivity to soil water variations. The contrary is observed over oceans. Snow covered areas are more sensitive to the XX polarisation, and this affects clearly the first-guess departures, because in these areas the CMEM modeled brightness temperatures are largely underestimated. A systematic negative bias is affecting the YY polarisation. The Southern Hemisphere presents more stable bias throughout the year, mainly because it is less affected by RFI and has a lower annual fraction of land covered with snow. North America shows very stable bias in the standard deviation, due to the switch off the main RFI sources in the northern part of the United States. South America show also very stable bias of the standard deviation. The bias are also very dependent on the incidence angle, as shown in the plots of the angular distribution of bias. In general, they increase in absolute value with the incidence angle for XX polarisation, whereas they are maximum at 30 degrees for YY polarisation. Note that CMEM parameterisation will be updated in the next ECMWF operational cycle 38R2 in June 2013. A different level of bias are expected.
Over continental surfaces, most of the figures show RFI contamination. The brightness temperatures standard deviation still present large anomalous values mainly over China, Middle East and Eastern Europe, with the YY polarisation being more affected than the XX polarisation. North and South America, most of Africa and Australia are quite clean from RFI. A significant degradation of the RFI situation was also observed during the last part of the summer in Central Europe due to the apparition of a strong source of RFI. Static sources of RFI are still remaining, but they are of less intensity and their contamination is limited to the surroundings of the source.

The current parameterisation of the ocean emission at L-band only accounts for the emission over a smooth surface of water, neglecting the wind and galactic noise components in the L-band emission. Therefore in this paper only statistics accounting for the observed brightness temperatures were reported. Observed brightness temperatures are much more homogeneous than for land pixels, as by nature oceans present less heterogeneities, and also present very different values compared to land, due to the very different dielectric constant of water. The polar regions present a clear contrast compared to the rest of the oceans, as these regions are affected by sea ice and snow cover, or a mixture of frozen and liquid water, with very different dielectric properties and brightness temperatures.

Acknowledgements

This work is funded under the ESA-ESRIN contract number 4000101703/10/NL/FF/fk and is the second (MR2) of a series of Monitoring Reports to ESA. The authors would like to thank Ioannis Mallas at ECMWF, for the operational acquisition and contribution to the processing of the data. Also many thanks to Rob Hine and Anabel Bowen, both ECMWF, for their great help with the figures shown in this report.

6 References

References

[1] G. Balsamo, P. Viterbo, A. Beljaars, B. van den Hurk, M. Hirschi, A.K. Betts, ja K. Scipal. A revised hydrology for the ECMWF model: Verification from field site to terrestrial water storage and impact in the integrated forecast system. *Journal of Hydrometeorology*, 10:623–643, 2009. doi: 10.1175/2008JHM1068.1.

[2] B. J. Choudhury, T. J. Schmugge, A. Chang, ja R. W. Newton. Effect of surface roughness on the microwave emission for soils. *Journal of Geophysical Research*, 84:5699–5706, 1979.

[3] P. de Rosnay, M. Drusch, A. Boone, G. Balsamo, B. Decharme, P. Harris, Y. Kerr, T. Pellarin, J. Polcher, ja J.-P. Wigneron. AMMA Land Surface Model Intercomparison Experiment coupled to the Community Microwave Emission Model: ALMIP-MEM. *J. Geophys. Res.*, 114, 2009. D05108, doi:10.1029/2008JD010724.

[4] P. de Rosnay, M. Drusch, ja J.Muñoz-Sabater. Milestone 1 Technical Note Part I: SMOS global surface emission model. Tekninen raportti, European Centre for Medium-Range Weather Forecast, Reading, United Kingdom, november 2009.

[5] M. Drusch, T. Holmes, P. de Rosnay, ja G. Balsamo. Comparing ERA-40 based L-band brightness temperatures with Skylab observations: A calibration / validation study using the Community Microwave Emission Model. *J. Hydrometeor.*, 10:213–226, 2009. doi: 10.1175/2008JHM964.1.

[6] M. Drusch, E. Wood, ja T. Jackson. Vegetative and atmospheric corrections for the soil moisture retrieval from passive microwave remote sensing data: Results from the southern great plains hydrology experiment 1997. *J. Hydrometeor.*, 2(2):181–192, 2001.

[7] T.R.H. Holmes, M. Drusch, J.-P. Wigneron, ja R.A.M. de Jeu. A global simulation of microwave emission: Error structures based on output from ECMWFS operational integrated forecast system. *IEEE Transactions on Geoscience and Remote Sensing*, 46(3, doi:10.1109/TGRS.2007.914798):846 – 856, 2008.

[8] K.P Kirdyashev, A.A. Chukhlantsev, ja A.M. Shutko. Microwave radiation of the earth's surface in the presence of vegetation cover. *Radiotekhnika i Elektronika*, 24:256–264, 1979.

[9] P. Matos ja A. Gutierrez. SMOS L1 processor discrete global grids document. Tekninen raportti, Deimos Engenharia, Lisboa, Portugal, 2004.

[10] J. Muñoz-Sabater, M. Dahoui, P. de Rosnay, ja L. Isaksen. SMOS Monitoring Report; Part II. Tekninen raportti, European Centre for Medium-Range Weather Forecasts, Reading, United Kingdom, December 2011.

[11] J. Muñoz-Sabater, P. de Rosnay, ja M. Dahoui. SMOS Continuous Monitoring Reports; Part I. Tekninen raportti, European Centre for Medium-Range Weather Forecasts, Reading, United Kingdom, February 2011.

[12] J. Muñoz-Sabater, P. de Rosnay, ja A. Fouilloux. Milestone 2 Technical Note, Part I:operational preprocessing chain, Part II:collocation software development, Part III: Offline monitoring suite. Tekninen raportti, European Centre for Medium-Range Weather Forecasts, Reading, United Kingdom, September 2010.

[13] J. Muñoz-Sabater, P. de Rosnay, ja G.Balsamo. Sensitivity of L-band NWP forward modelling to soil roughness. *Int. J. Remote Sens.*, 32(19):5607–5620, 2011. iFirst 2011., doi: 10.1080/01431161.2010.507260.

[14] T. Pellarin, J.-P. Wigneron, J.-C. Calvet, ja P. Waldteufel. Global soil moisture retrieval from a synthetic l-band brightness temperature data set. *Journal of Geophysical Research*, 108(4364, doi:10.1029/2002JD003086), 2003.

[15] R. Salgado. Global soil maps of sand and clay fractions and of the soil depth for MESONH simulation based on FAO/UNESCO soil maps. Tekninen raportti, CNRM/Météo France, 1999. Tech. Note, **59**.

[16] J. R. Wang ja T. Schmugge. An empirical model for the complex dielectric permittivity of soils as a function of water content. *IEEE Transactions on Geoscience and Remote Sensing*, 18:288–295, 1980.

[17] J.-P. Wigneron, Y. Kerr, P. Waldteufel, K. Saleh, M.-J. Escorihuela, P. Richaume, P. Ferrazzoli, P. de Rosnay, R. Gurneye, J.-C. Calvet, J.P. Grant, M. Guglielmetti, B. Hornbuckle, C. Mtzler, T. Pellarin, ja M. Schwank. L-band microwave emission of the biosphere (L-MEB) model: Description and calibration against experimental data sets over crop fields. *Remote Sensing of Environment*, 107(4):639–655, 2007.

[18] J. P. Wigneron, L. Laguerre, ja Y. Kerr. A simple parameterization of the L-band microwave emission from rough agricultural soils. *IEEE Transactions on Geoscience and Remote Sensing*, 39:1697–1707, 2001.